POLITECNICO DI TORINO

Master of Science in Energy and Nuclear Engineering

Master Thesis

Simulation and Analysis of Cryomodule Heat Loads and Cold Test for the High Beta 650 MHz Prototype in the PIP-II Project

Advisors

prof. Roberto BONIFETTO, Ph.D.

prof. Parisa MIRBOD, Ph.D.

Supervisor

Vincent ROGER, M.Sc.

Candidate

Giuditta COLADONATO

Abstract

The Proton Improvement Plan II (PIP-II) project at Fermilab aims to upgrade the particle accelerator complex to generate high-energy neutrino beams for the Deep Underground Neutrino Experiment (DUNE) and the Long-Baseline Neutrino Facility (LBNF). As part of this project, the design and optimization of the cryomodules play a crucial role in achieving efficient operation. In this thesis, the focus is on the High Beta 650MHz (HB650) cryomodule, which was chosen for detailed analysis due to its relevance during the research period. The aim of this study is to estimate the heat loads, and determine the temperatures of key components during cool-down. To accomplish this, Simulink (MATLAB) has been used on a simplified geometry to simulate HB650 cool-down from 300 K to 2 K, the simulation results are then compared with the actual cold test data obtained from the prototype HB650 cryomodule. This comparative analysis provides insights into the cryomodule's performance and helps validate the simulation models. The findings from this research contribute to the overall understanding and optimization of the cryomodule design for the PIP-II project, aiding in the development of efficient cryogenic systems for future particle accelerator operations.

Summary

Table of figures

Table of tables

1. Introduction

1.1. PIP-II

The PIP-II project represents a crucial advancement in Fermilab's particle accelerator complex, aiming to transform the facility into a global leader in accelerator-based neutrino research. The groundbreaking for this ambitious upgrade took place in March 2019, with the primary objective of generating an unparalleled stream of neutrinos, fundamental particles that hold vital clues about the evolution of the universe. By creating the world's most intense high-energy neutrino beams, Fermilab will enable groundbreaking scientific investigations in collaboration with the international Deep Underground Neutrino Experiment (DUNE) and Long-Baseline Neutrino Facility (LBNF).

Central to the success of PIP-II is the focus on increasing power. Once the project is completed, Fermilab will have the capability to generate proton beams exceeding 1 megawatt, a remarkable 60% increase compared to current capabilities. These powerful proton beams will, in turn, produce highly intense neutrino beams. Additionally, future upgrades to PIP-II will triple the current beam power, solidifying Fermilab's position as a leading center for accelerator-based particle physics research.

A distinguishing aspect of PIP-II is its collaborative nature, with significant contributions from international partners. Institutions from France, India, Italy, Poland, and the UK are expected to contribute their expertise in accelerator technologies, drawing upon their successful participation in international accelerator projects. Leveraging Fermilab's pioneering work in superconducting technology for particle acceleration, PIP-II will incorporate cutting-edge advancements, raising the performance of the next generation of accelerators.

The high-intensity neutrino beams generated by the powerful PIP-II-enabled accelerator complex will embark on a remarkable journey (Fig.1). They will first reach the initial DUNE particle detector located within the Fermilab site. Subsequently, these neutrinos will travel a distance of 800 miles (1,300 kilometers) through Earth's mantle to reach a second, significantly larger detector situated a mile underground at the Sanford Underground Research Facility in Lead, South Dakota. By comparing data from both detectors, scientists will gain valuable insights into the behavior of neutrinos as they traverse long distances, unlocking the mysteries surrounding their transformations. [1]

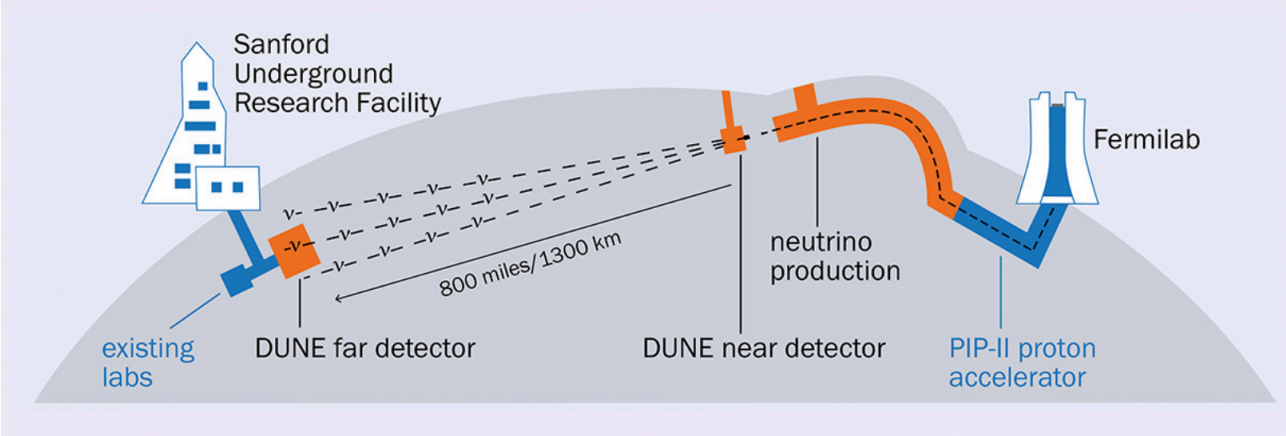

Figure 1: Neutrino beamline and DUNE near detector hall at Fermilab [2].

High energy particle accelerators have a preference towards adopting superconducting radio frequency (SCRF) technology because of its inherent advantages. This technology greatly increases the energy per unit length of the accelerating components of accelerators, resulting in more powerful and smaller machines.

In a linear particle accelerator (LINAC), particles undergo acceleration in a straight trajectory with a target positioned at one end. The LINAC has an ion source, which produces H- ions. These ions have one proton and two electrons and are then injected into accelerator for

acceleration to higher energies. [3] After reaching higher energy states in LINAC, the ions then pass through a foil, which strips off each ion's two electrons, converting it to a proton. The protons pass into a ring-shaped structure, a proton accumulator ring, where they accumulate in “bunches”, each bunch of protons is released from the ring as a pulse, at a rate of generally 60 times per second (60 hertz) but, this rate may vary for different accelerators. This bunches of high energy protons are used to generate neutrons. The high-energy proton pulses strike a target, where spallation occurs. The spalled neutrons are then decelerated in a moderator and guided through beam lines to areas consisting special instruments, where they are utilized for a variety of experiments.

High-energy linear accelerators utilize a linear arrangement of plates or drift tubes, subjecting them to alternating high-energy fields. When particles approach a plate, they experience acceleration towards it due to an opposite polarity charge applied to the plate. As they pass through a hole in the plate, the polarity is switched, causing the plate to repel the particles and propel them towards the next plate for further acceleration.

As particles travel near the speed of light, the rapid switching of electric fields reaches radio frequencies. To accommodate this, higher energy accelerators employ microwave cavities instead of simple plates. These cavities serve as the means to generate and control the necessary electromagnetic fields for accelerating particles effectively.

The PIP-II LINAC is 215 meters long and its components [4] (Fig.2) include:

Ion sources: The baseline design of the PIP-II Linac include two H- sources**,** located on the far left side of Fig.2**.** A filament placed inside a chamber filled with hydrogen gas, provides the electrons that turn neutral hydrogen molecules into negatively charged particles because only charged particles can be accelerated by the electric fields used in the accelerator.

RFQ (Radio Frequency Quadrupole Accelerator): RFQ, shown in Fig.2, after the Ion source, is designed to accelerate the beam to 2.1 MeV. As the beam exits the RFQ device a series of magnets further focuses the beam and keep the particles from straying the center line.

Next the particles enter in the superconducting section of PIP-II, which is always powered by radiofrequency waves in cavities made of niobium. These cavities ,when cooled to -271 º by the cryoplant and CDS (Cryogenic Distribution System) , they propel particles much more efficiently because the niobium conducts electricity without resistance. The cavities are installed inside cryomodules, these are large cryogenic vessels that insulate the cavities and surround them with liquid helium to keep them at ultra-cold temperature.

SRF Linac: The SRF LINAC is designed to accelerate H beams and consists of five different types of cavities. The number of cavities and their design are optimized to match the velocity profile of the accelerated H- beam. The biggest difference between these modules is the shape of the cavity. As the beam accelerates, new cavity geometry is required to optimize the electro-magnetic field for higher velocities and acceleration. The first cryomodule of PIP-II is HWR (Half Wave Resonator) and operates at 162.5 MHz. In the next stage , that includes 9 cryomodules SSR (Single Spoke Resonator), the radio frequency doubles to 325 MHz and the shape of niobium cavities change as well (Single Spoke Cavities). When the particles exit this stage of PIP-II they are traveling at 54% of the speed of light. [5]

The final and the longest part is the superconducting section is a set of 13 cryomodules (Low Beta 650 MHz and High Beta 650 MHz). The particles traverse this final section in less than one millionth of a second. Here cavities that operate at a radio frequency of 650 megahertz are used. These cavities feature a different elliptical shape to optimize the energy transfer to the speedier particles. Exiting this section particles travel at 84% of the speed of light.

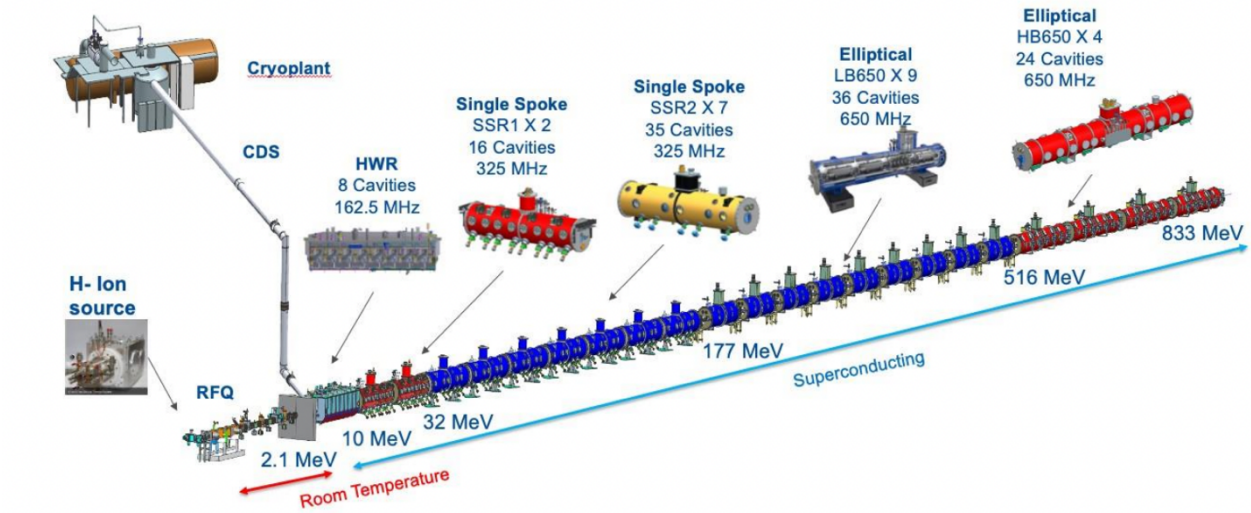

Figure 2: LINAC cryomodule arrangement. [6]

The focus of this thesis is the cryomodule HB650 MHz, which constitutes the final section of the LINAC.In early 2023, the assembly of the prototype HB650 (Fig.3) cryomodule was completed and the cold tests started to evaluate its performance.

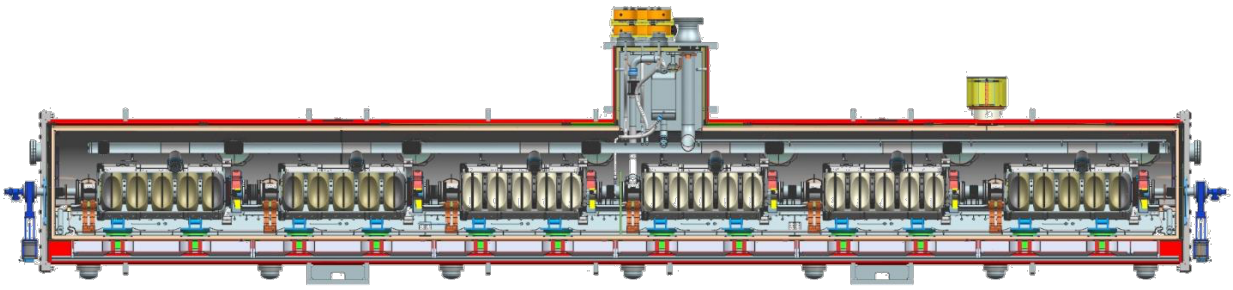

Figure 3: HB650 cryomodule.

Precise estimation and optimization of cryogenic efficiency are crucial for the successful operation of cavities working at cryogenic temperatures. Superconducting cavities offer significant power savings due to their ability to operate at extremely low temperatures. During the prototyping phases, it becomes essential to accurately estimate the performance and

efficiency of these cavities in order to identify areas for improvement. The low temperature of 2 K poses unique challenges, as cryogenic efficiency is significantly lower in this range [7]. Consequently, the size and cost of the required cryogenic plant are directly influenced by the demands of operating at such temperatures.

Over the last years, calculations have been done to estimate the heat loads of the PIP-II LINAC in order to design the appropriate cryogenic plant and the cryogenic distribution system [8]. In the framework of the MINERVA (MYRRHA 100 MeV) project, previous studies successfully analyzed the heat loads using MATLAB Simulink [9] and demonstrated a strong estimation of the overall efficiency. A Simulink library of cryogenics components presented in the article [10] provides a comprehensive set of components, such as valves, phase separators, mixers, and heat exchangers, which can be assembled to generate model-based control schemes. The models generated using this library can facilitate the design of advanced model-based control schemes, including constrained model predictive control, which is particularly valuable for cryoplants experiencing large pulsed thermal loads. In the field of cryogenics, particularly in large-scale projects like ITER, various tools and software platforms are employed to analyze and simulate complex systems. One such tool commonly used is Modelica [11], a modeling language that allows for the efficient representation of physical systems and their dynamic behavior. Modelica offers a comprehensive framework for modeling and simulating cryogenic systems, enabling researchers and engineers to investigate and optimize the performance of cryogenic components and processes. Its capabilities extend to the analysis of thermal behavior, heat transfer, fluid dynamics, and other relevant phenomena encountered in cryogenic applications. By utilizing Modelica and similar tools, researchers in the cryogenic field can enhance their understanding and design of advanced cryogenic systems, contributing to the successful development and operation of projects such as ITER. [12]–[18]

1.2. Aim of the work

The aim of this thesis is to investigate and analyze the thermal behavior of the HB650 cryomodule components, which have been specifically chosen as the focal point of the research. The selection of the HB650 cryomodule was based on the availability of relevant data, as it had undergone the cooling down and testing process during the timeframe of this thesis. By utilizing the Simulink/Simscape model, the focus is on accurately estimate the heat loads and understanding the thermal dynamics of the cryomodule system. Heat transfer through conduction can usually be estimated precisely, but estimation of the radiative heat load in a cryomodule is non-trivial and strongly affected by the geometry and physical properties of a surface. Therefore, a key objective of this research is to develop an improved calculation method for accurately determining the radiative contribution to the heat loads. The precise estimation of heat loads is essential for optimizing the cryogenic efficiency and overall performance of the cryomodule during its operation at cryogenic temperatures. Additionally, this research aims to validate the Simulink/Simscape model by comparing the temperature evolution of each component with corresponding experimental data, ensuring the accuracy of the model's predictions. The findings from this thesis will contribute to the ongoing efforts to enhance the efficiency and performance of the HB650 cryomodule.

2. HB650 design

The cryomodule is illustrated in Fig.4, which includes the following main components listed from the bottom to the top: vacuum vessel, strongback, G11 support posts, thermal shield, cavity supports, cavity, two-phase pipe, and relief line. [19]

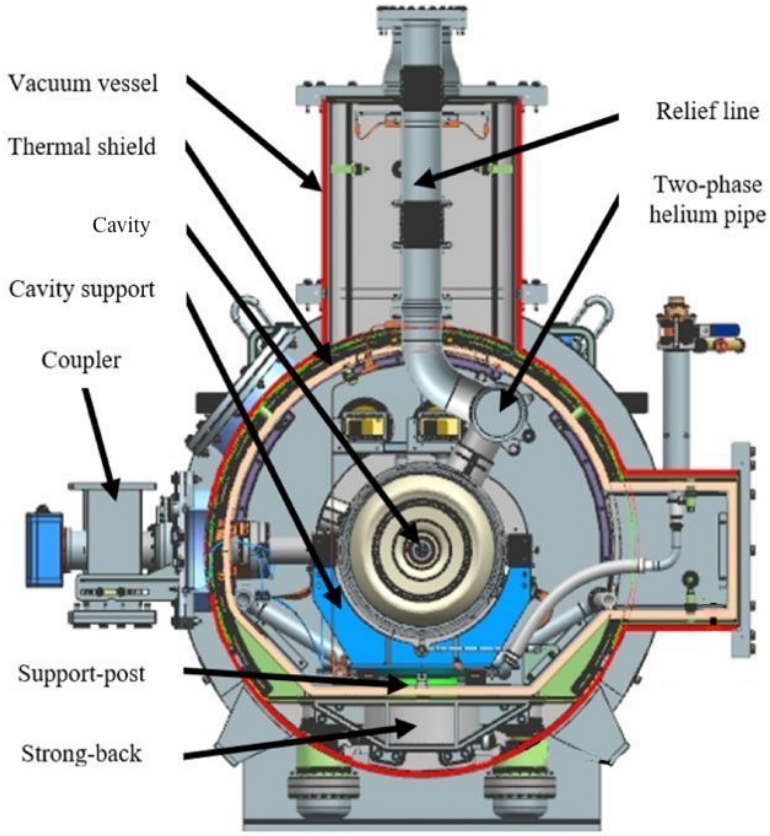

Figure 4: Cross-section of the HB650 cryomodule.

Flexible thermal linkages (Fig.5), such as thermal straps, have been widely employed in various cryogenic systems [20] to address the need for efficient heat transfer between components while also accommodating thermal contractions and isolating mechanical vibrations. These thermal linkages are designed to provide high thermal conductance, allowing for effective temperature regulation and minimizing the impact of thermal gradients on system performance. For the HB650 cryomodule, various thermal straps were utilized, each

featuring different contact areas and braid lengths. In all cases, the thermal straps were constructed with a braid composed of fine copper strands that were cold-pressed at both ends using slotted copper blocks, known as end-lugs. The pressing procedure was performed using a mechanical press under open atmosphere conditions. Both the braid and end-lugs were fabricated from 99.98% pure oxygen-free high thermal conductivity (OFHC) copper, ensuring optimal thermal performance and conductivity throughout the cryomodule system.

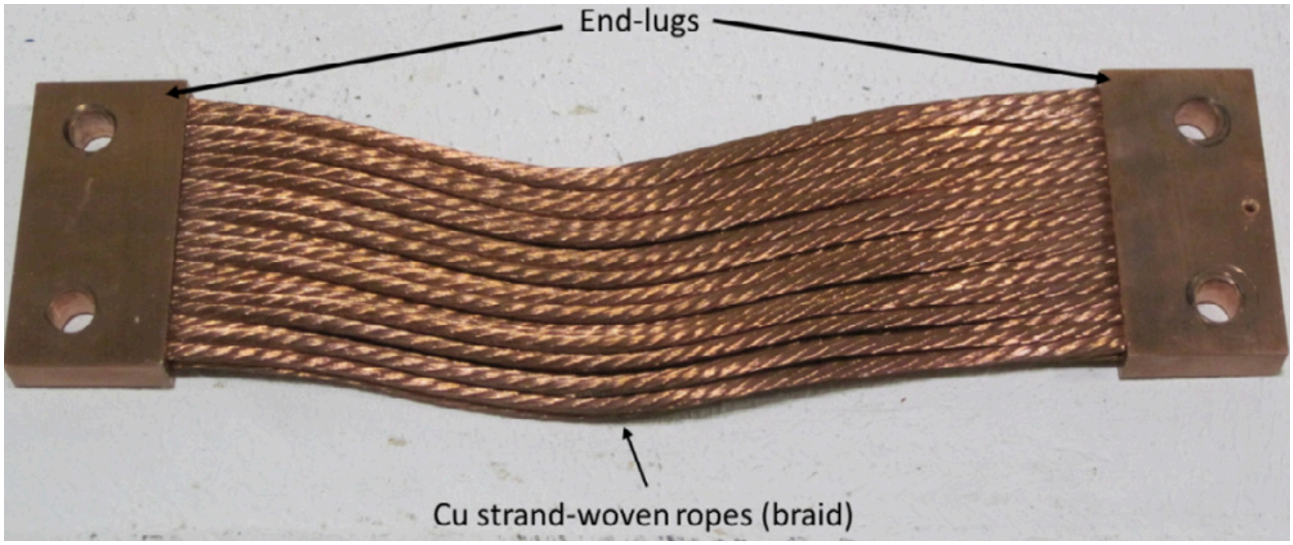

Figure 5: Photograph of a Copper Thermal Strap displaying the copper strand-woven rope braid and the end-lugs. [21]

2.1. Vacuum Vessel

The vacuum vessel (Fig.6) consists of a cylindrical shell in carbon steel anchored to the floor with bottom supports and equipped with lugs for lifting purposes; several bolted and sealed flange ports through the vacuum vessel wall provide access. The vessel shell is closed at the upstream and downstream sides with endcaps, and it has ports for input RF power couplers, access, instrumentation, vacuum pump-out, and safety relief. This exterior shell remains at room temperature and for this reason the vacuum vessel emits heat that irradiates onto the thermal shield when it's cooled down. Furthermore, vacuum vessel provides the first

obstacle to heat transfer to the supercooled beamline since the vacuum precludes transmission of heat transfer between the exterior shell and the interior components by convection.

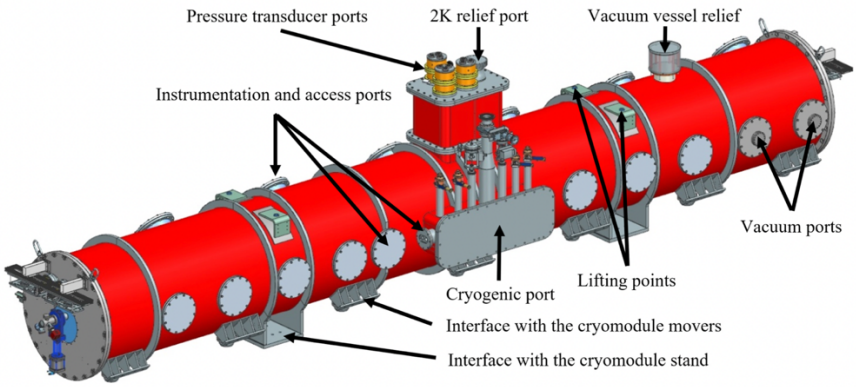

Figure 6: Vacuum Vessel.

2.2. Strongback

The strongback (Fig.7) is a key component of the cryomodule. It plays an important role in transportation since it supports the weight of the entire cold mass and provides stable alignment of the string; it consists of an Al-6061 T6 extrusion bolted to two carbon steel parallel rails. Since the strongback is connected to a warm source (the vacuum vessel through studs) and cold sources (the support posts of the cavities and the thermal shield), maintaining it at room temperature may be a challenge. To increase the heat exchange by radiation between the vacuum vessel and the strongback, the lower surface of the strongback is sand-blasted and the inner surface of the vacuum vessel is covered by epoxy. Therefore, both surfaces are expected to have an emissivity around 0.7. In addition, 14 thermal straps connect the strongback to the vacuum vessel.

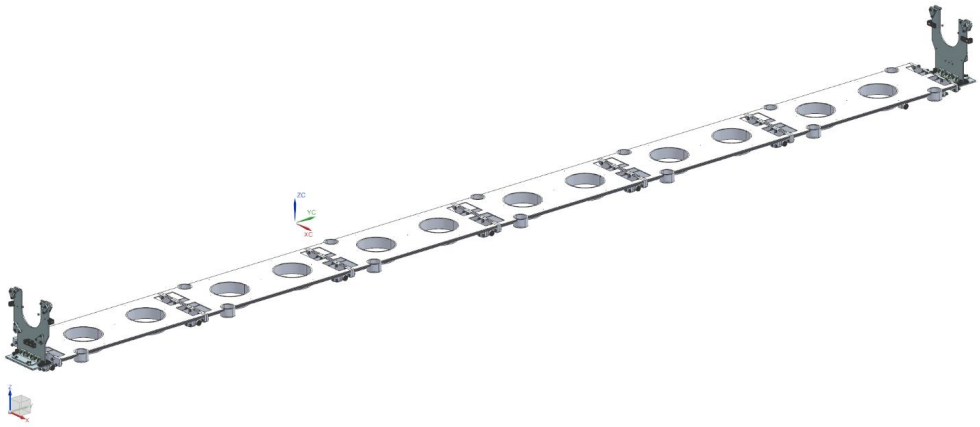

Figure 7: Strongback.

2.3. Support Post and Cavity Support

The G11 support post (Fig. 8a) located below the cavity support is designed to support the cold mass and to isolate the strongback from the cold mass. The G11 is a thermosetting composite material made with glass fibers and epoxy resin as a matrix. These posts transfer conductive heat with the strongback and the HTTS with two thermal straps. Each titanium cavity support (see Fig. 8b), positioned on top of the G11 support posts, has two thermal straps connected to the LTTS pipe. Additionally, the radiation from the cavity support to the cavities has been considered. It is important to note that there are a total of 12 support posts, with two support posts assigned to each cavity.

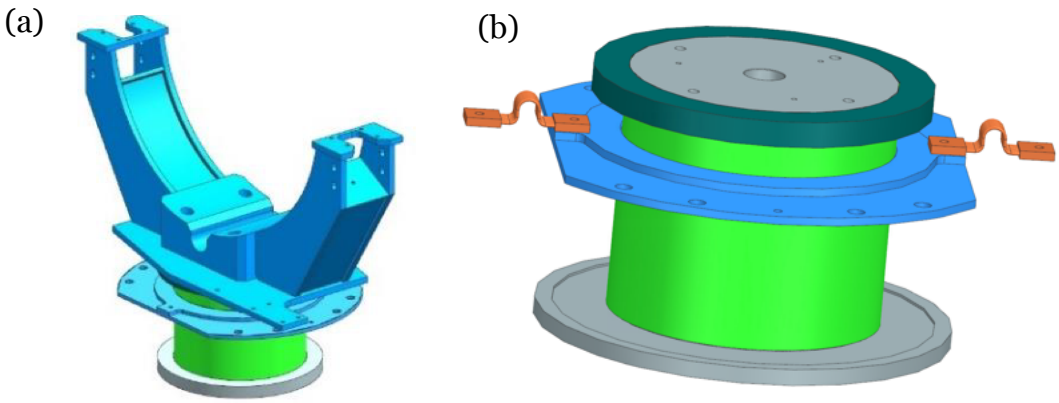

Figure 8: Cavity support on the support post (a) and Support post (b)

2.4. Thermal Shield

The HTTS (High Temperature Thermal Shield) (Fig.9) is used to shield the heat loads by radiation from the vacuum vessel and to intercept heats by conduction on several components such as the support posts, couplers, relief line, pressure transducer lines, bayonets and cryogenic valves. The HTTS is composed of aluminum alloy Al 1100-H12 for the sheets and aluminum alloy Al 6061 T6 for the extrusion (the pipe carrying the helium gas). The extrusion is welded to the HTTS sheets by means of finger welds, which are designed to reduce thermal stresses during the cooldown.

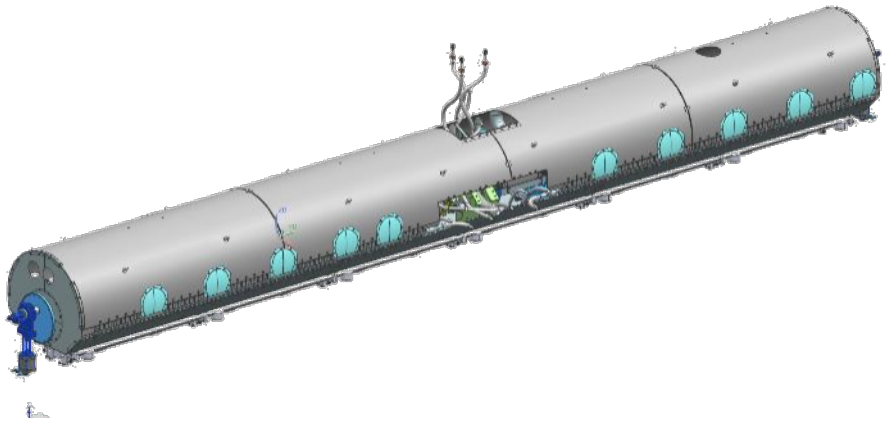

Figure 9: Thermal Shield.

The thermal shield is divided into 4 different parts: Lower Thermal Shield, Upper Thermal Shield, Edge Thermal Shield and Side Thermal Shield, as described in Fig.10. The lower and upper parts of the thermal shield are welded to the extruded pipe, ensuring a secure attachment. The side thermal shield, on the other hand, is thermally connected to the lower thermal shield using thermal straps and secured in place with screws. Lastly, the edge thermal shield is welded directly onto the upper thermal shield, providing a robust connection between the two components.

The HTTS is convection cooled by helium gas flowing in the HTTS extrusion pipe (Fig.12).

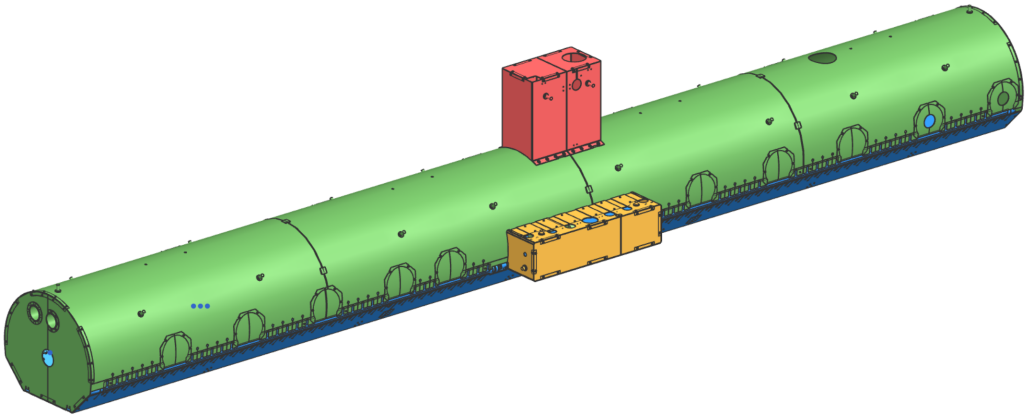

Figure 10: Thermal Shield Partitions. In blue, the lower thermal shield, in green the upper thermal shield, in red the top part of the shield and in orange the side part of the shield.

The thermal shield is covered by 30 layers of insulation (MLI) (Fig.11) , which serves to reduce the radiative heat transfer between the shield and the vacuum vessel at ambient temperature.

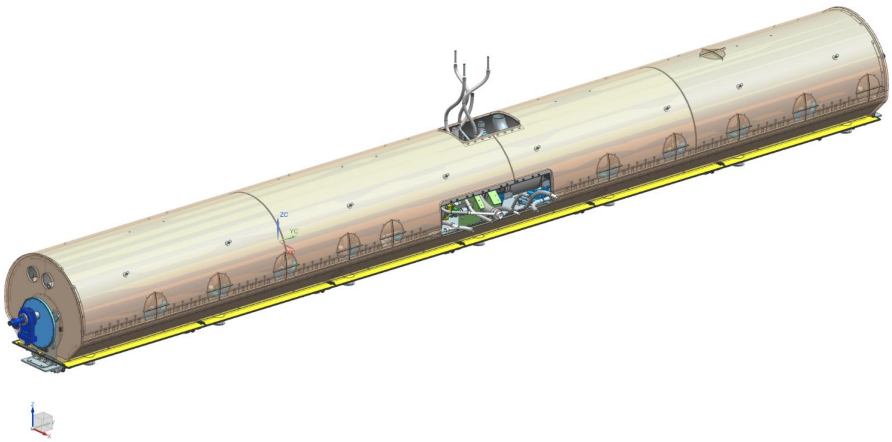

Figure 11: Thermal shield with MLI.

The upper thermal shield and lower shield are both welded to the HTTS extruded pipe by means of finger welds (Fig.12), which are designed to reduce thermal stresses during the cooldown [19]. The finger welds are the red triangular prisms shown in the Fig. 12 and they are made of the same material of the thermal shield (Al 6061 T6) .[19]

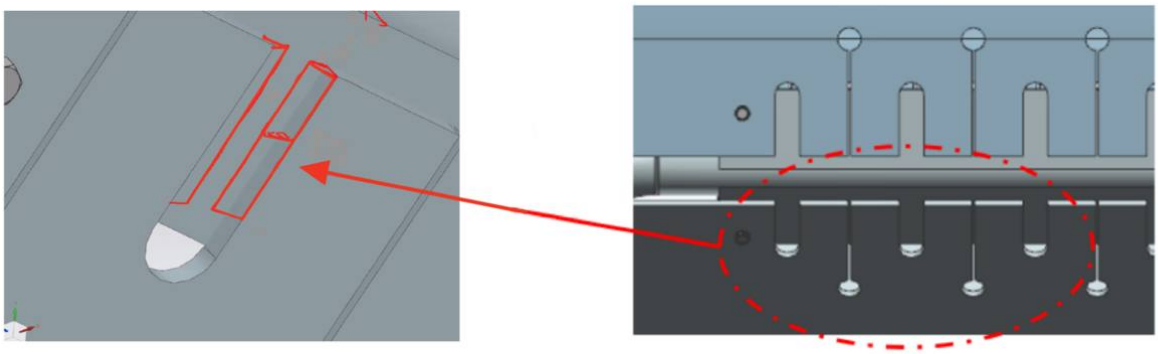

Figure 12: Welds.

2.5. LTTS

A Low Temperature thermal source (LTTS) (Fig.13) is being used as a thermal intercept for the beam line, couplers, relief line and support posts. The LTTS consists of a pipe made of Al 6061 T6 and it is equipped with three bayonets. Bayonets are special rotary connectors used to facilitate translational movements of cryogenic and vacuum service lines, allowing for electrical isolation along the piping.

Figure 13: LTTS Line

2.6. Couplers

RF input power couplers have two main functions: transferring RF power from the source to the load and acting as a barrier between the gas-filled transmission line and the vacuum cavity; furthermore, they minimize heat loads when transitioning from room temperature to cryogenic temperatures inside the cryostat [22]. In Fig. 14 the section of a coupler is shown; each cavity has one coupler.

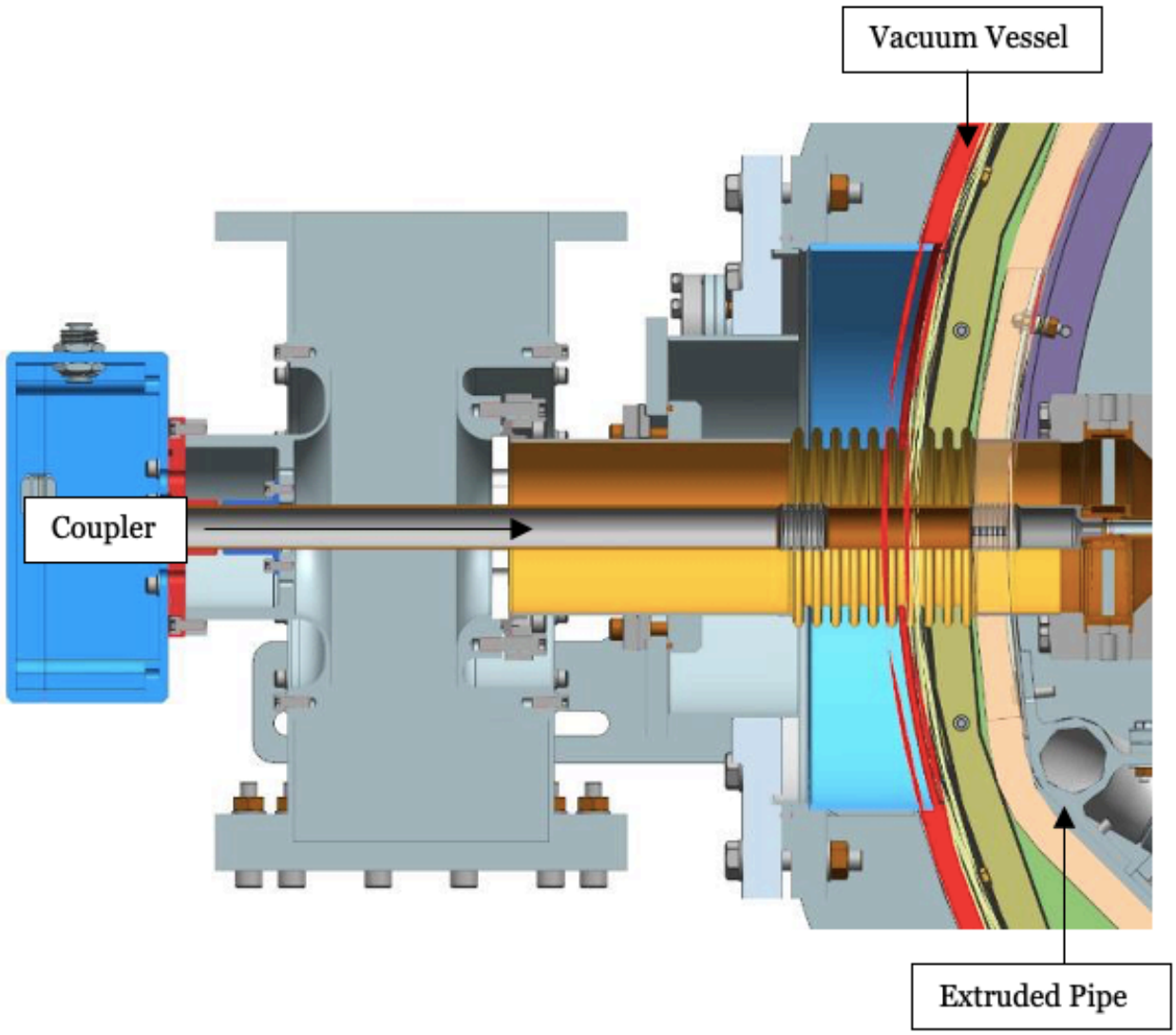

Figure 14: Coupler section.

2.7. Relief Line

The relief line shown in Fig.15 is used to protect against cryomodule failure scenarios [23], as accidental helium discharges, usually the baseline design choice for the helium recovery system is a set of safety valves connected to a relief line that ends in a gas bag. The relief line in a cryogenic system is a significant component that necessitates careful consideration due to its role in managing heat loads. Structurally, the relief line consists of multiple sections, each with distinct thermal characteristics. The initial part of the relief line is maintained at ambient temperature, serving as a transition between the cryogenic environment and the

surrounding conditions. This section facilitates the dissipation of heat and ensures a controlled thermal gradient. To effectively manage heat transfer, the relief line is thermally connected to the thermal shield using thermal straps, which enable efficient heat transfer between the two components. The subsequent segment of the relief line extends to the 2K pipe, which operates at cryogenic temperatures, with a junction of the two 316 stainless steel. This section is subject to lower temperatures and, consequently, presents unique challenges in heat management. Figure 14 provides an illustration of three flex hoses, which serve as flexible pipes to accommodate the passage of instrumentation wires. These flex hoses are strategically designed to mitigate the thermal effects on the wires. To achieve this, the flex hoses are thermally connected to both the High-Temperature Thermal Shield (HTTS) and the Low-Temperature Thermal Shield (LTTS) through thermal straps. Furthermore, the end of the flex hoses, similar to the relief line, is directly connected to the 2K line, ensuring efficient heat transfer and maintaining thermal equilibrium.

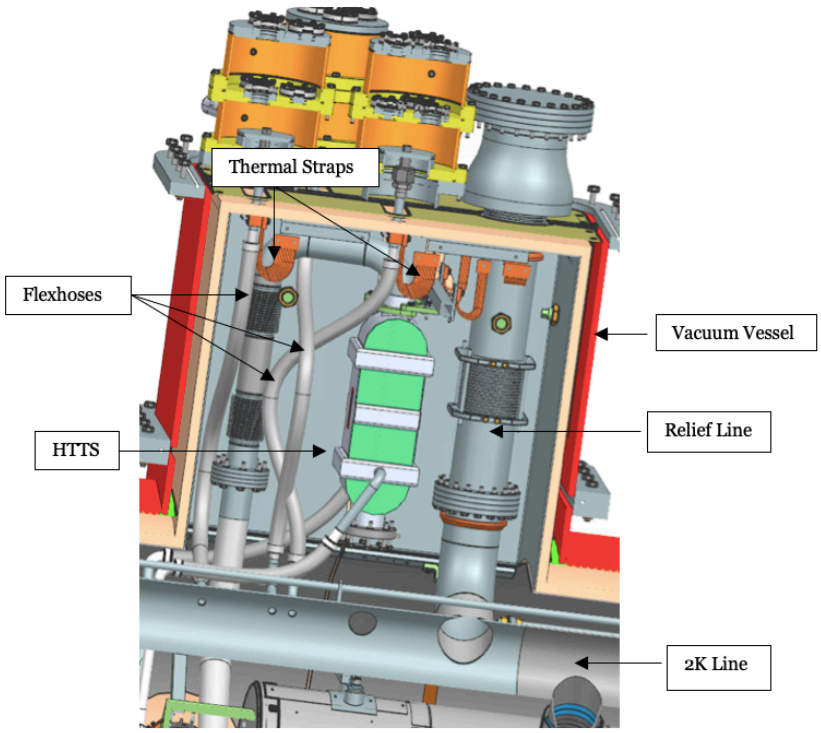

Figure 15: Relief line and Flex hoses.

2.8. Cavity and Two-Phase Pipe

In HB650 cryomodule there are six cavities installed (Fig.16) and each is divided into two parts, the actual niobium cavity that has the purpose of accelerating the beam using magnetical resonance, and the external helium vessel, composed of titanium, which contains the helium used to refrigerate the niobium cavity in order to make the cavities superconductive.

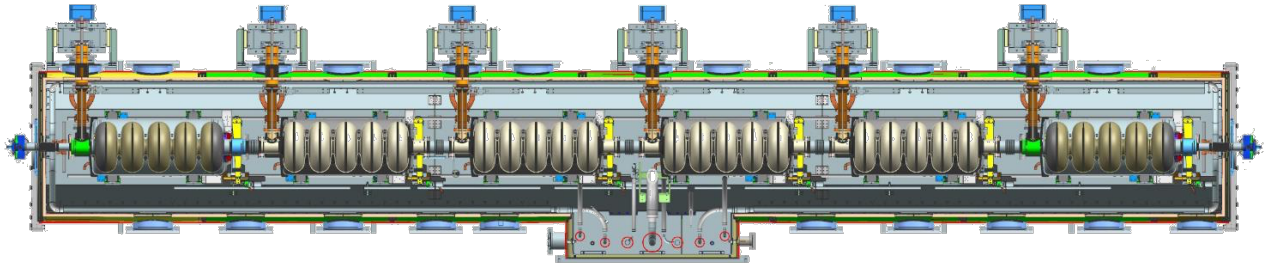

Figure 16: Cryomodule section.

The cavities, located in the middle of the coldmass, are cooled down by the cool-down line. Each cavity is indirectly connected to a coupler through a stainless-steel pipe, serving as a thermal resistance. Moreover, the radiation from the HTTS to the cavities has been considered. Based on the design of the interface in between the cavity support and the cavity, it has been decided to consider that there was no heat-exchange in between these parts. In Fig. 17a the cavity vessel and the two phase pipe and connections between cavities are shown while in Fig. 17b the section of cavity is shown.

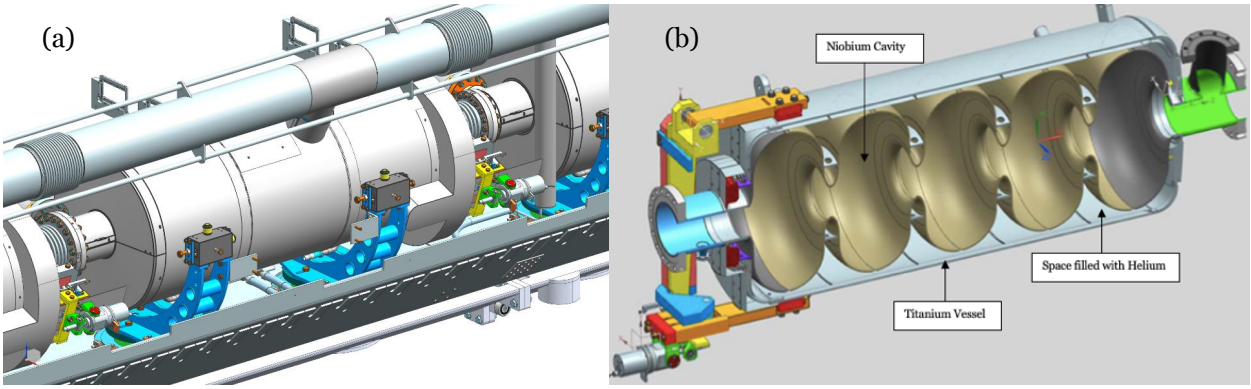

Figure 17: Cavity and 2K Line (a) and Section of the Cavity (b)

3. Cooling

The PIP-II HB650 cryomodules are designed adopting the Fermilab style cryomodule that uses a room temperature strongback as foundation. This design choice is part of a design strategy [24] that was defined by the project to standardize parts in between cryomodules [25]. Fig. 18 describes the cryomodule layout of the HB650 cryomodule. A cool-down valve is used to cool-down the cavities up to 4K, then an heat exchanger, Joule Thomson valve and pumping line are used together to reach 2K.

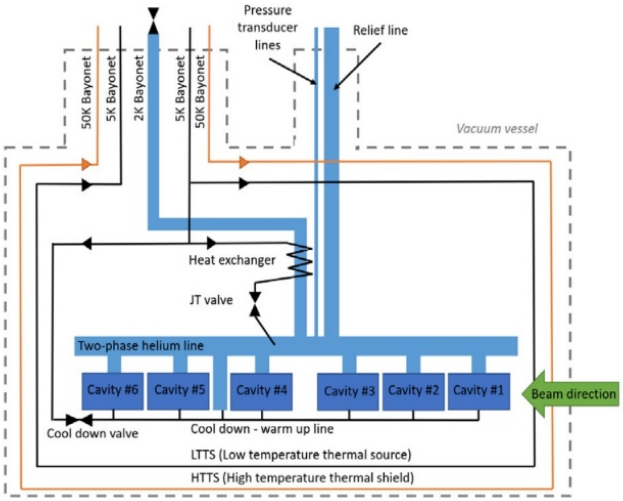

Figure 18: HB650 cryomodule layout.

3.1. Cool-down procedure

The cool-down of the cryomodule is done using a detailed procedure to operate safely the cryomodule and reach the appropriate performance. First only the thermal shield is cooled down from room temperature to 50K by maintaining a maximum temperature difference of maximum 100K across the shield. Fig. 19 presents the temperature data collected from the sensors located on the edge thermal shield, upper thermal shield, lower thermal shield, and side thermal shield during the HTTS cooldown of the HB650 MHz cryomodule. These sensors were strategically positioned to capture the temperature variations across different regions of the thermal shields throughout the entire cooldown process. The detailed analysis and interpretation of these sensor measurements will be discussed in section 3.2. The

cooldown process took place from 1st March at 10 AM to 3rd March at 11 AM in the cryomodule test facility at Fermilab.

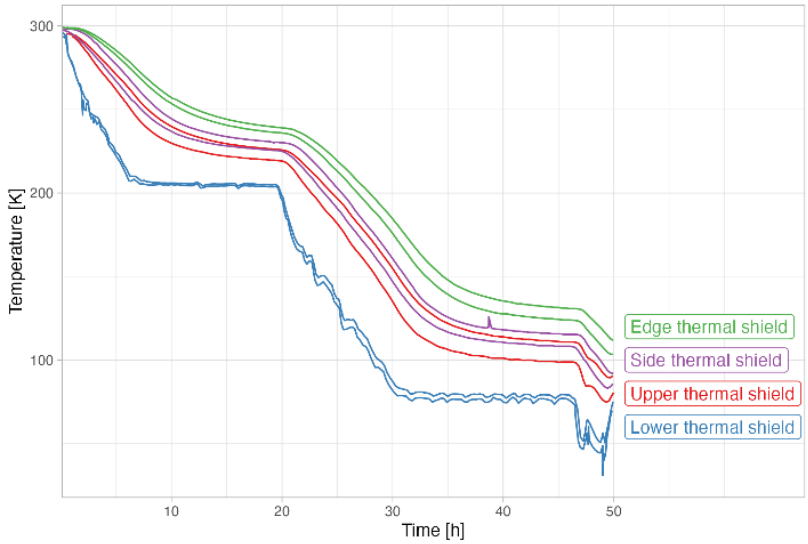

Figure 19: Cool-down of the HTTS.

While maintaining closed the outlet of the LTTS and open the cool-down valve, the cavities are cooled to 4K. The requirement is to go as fast as possible and to ensure a minimum rate of 20 K/h between 175K and 90K. The next step is to open the outlet of the LTTS, cooling down many thermal intercepts and reducing the 2K heat loads. Finally, the cool-down valve is closed, and the Joule Thomson valve is open to reach 2K.

This cryomodule being a prototype, it has been decided to close the helium inlets during the night for safety reasons. That is why the curves on the Fig. 19 show two plateaus. Fig. 20 illustrates the temperature evolution of the cavities during the cooldown process to 4K (prior to the opening of the 2K valve). The cooldown procedure took place from the 6th of March at 9 AM to the 8th of March at 9AM (48 hours), spanning a total duration of 48 hours. Two temperature sensors were employed in the cavities, one positioned in the bottom part and the other in the top part (Fig.21). As helium flows from the bottom of the cavity, the bottom part was naturally the first to undergo cooling, as evident from the observations depicted in the figure. Furthermore, it is important to note that the second cooldown did not occur

immediately after the first one. This period allowed for careful evaluation of the controls and parameters involved, ensuring that the subsequent cooldown could be executed without issues.

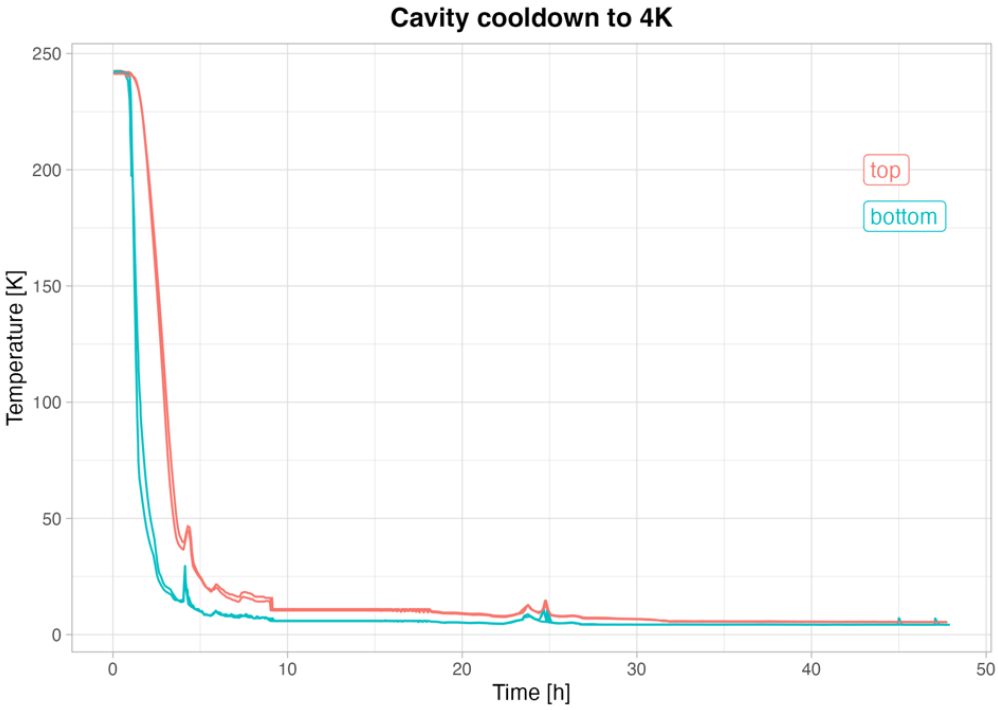

Figure 20: Cool-down of the cavity to 4 K.

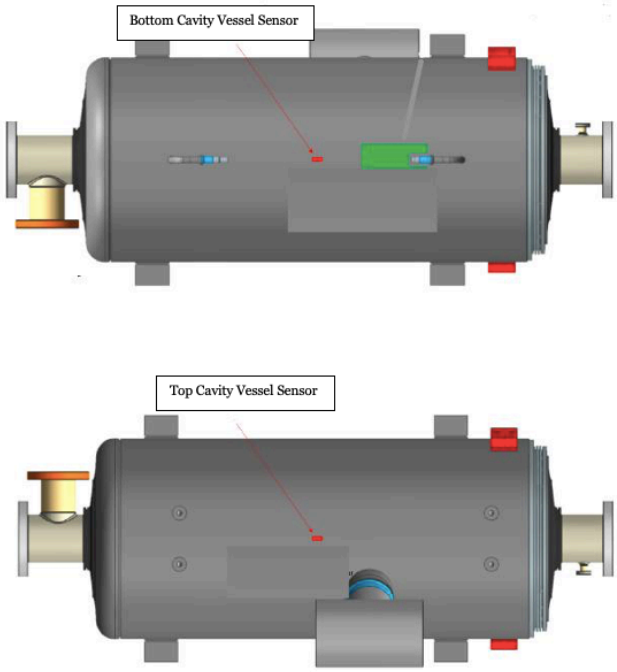

Figure 21: Top and Bottom Cavity Sensors.

Fig. 22 illustrates the cool down of the cavities to 2K, specifically exhibiting the temperature measurements obtained from the top and bottom cavity sensors. This cooling process, driven by the Joule-Thomson valve, commenced immediately after the previous cooldown. The duration of this phase spanned from 9 AM on the 8th of March to 2 PM on the same day, signifying a relatively rapid cooling period.

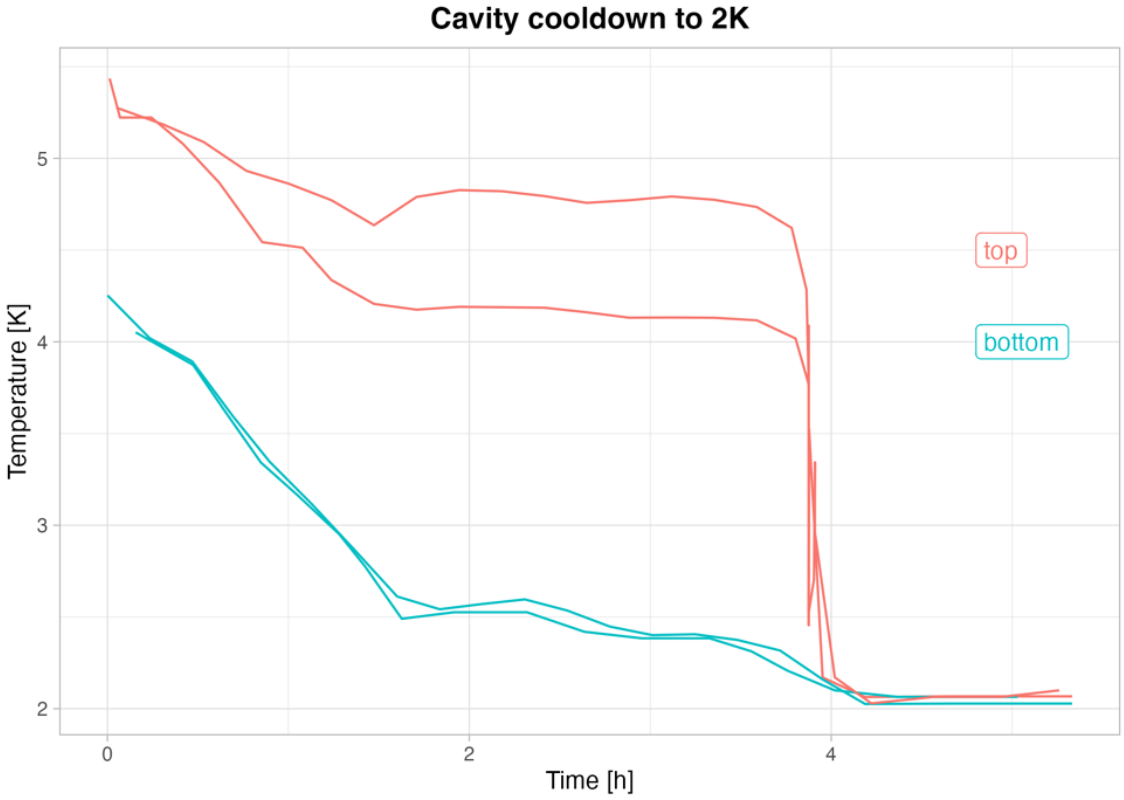

Figure 22: Cool-down of the cavity to 2K.

The validation of the model primarily focused on the first cooldown due to limitations in data collection during the second and third cool downs when the components reached cryogenic temperatures. As a result, the second and third cooldowns were not included in the validation process. However, plans are underway to conduct a second cooldown at the end of July, which will provide an opportunity to further validate the model for the entire cooling process. This additional validation will enable a comprehensive assessment of the model's

accuracy and performance in capturing the dynamic behavior of the system throughout the entire cooldown period.

3.2. Sensors position

To validate the accuracy of the model and verify the thermal resistances incorporated within it, a comparative analysis was conducted by observing the cooling down process of specific components. The temperature evolutions of these components were obtained from the experimental data and compared with the corresponding output from the model. To obtain the necessary experimental data for validation, temperature sensors were strategically placed and monitored during the cooldown process of the HB650 cryomodule. These sensors allowed for the precise measurement and analysis of the temperature variations experienced by the components.

To effectively monitor the temperature of the lower thermal shield, a comprehensive sensor arrangement was implemented with four temperature sensors (Fig.23).

The first sensor was positioned to monitor the inlet temperature of the helium as it passed through the extruded pipe, which played a vital role in cooling down the lower thermal shield. A second sensor was placed at the outlet of the extruded pipe to monitor the temperature of the helium as it exited the system. This measurement was crucial in assessing the effectiveness of the cooling process and understanding the temperature changes experienced by the helium during its passage through the system. Additionally, two sensors were directly attached to the extruded pipe itself. This placement allowed for the direct measurement of the pipe's temperature in two different locations, which closely represents the temperature of the lower thermal shield. By directly monitoring the extruded pipe's temperature, the measurements obtained provided a reliable representation of the temperature of the lower thermal shield, ensuring that the lowest possible temperature was captured (being it the temperature of the heat sink).

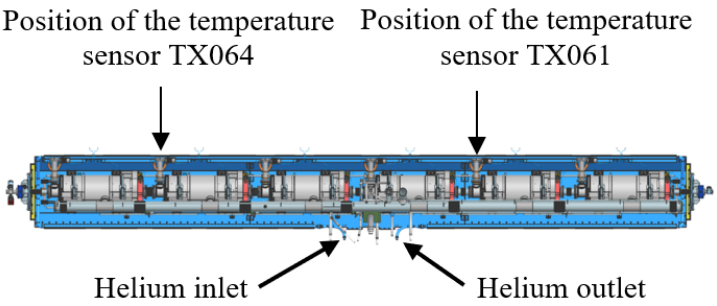

Figure 23: Temperature sensor positions on the pipe cooling the lower thermal shield.

To accurately monitor the thermal behavior of the edge thermal shield, TX-066 and TX-067 were strategically placed to capture its temperature evolution.

The placement of these two sensors (Fig.24) was carefully chosen to ensure that they provided an accurate representation of the thermal characteristics of the edge thermal shield.

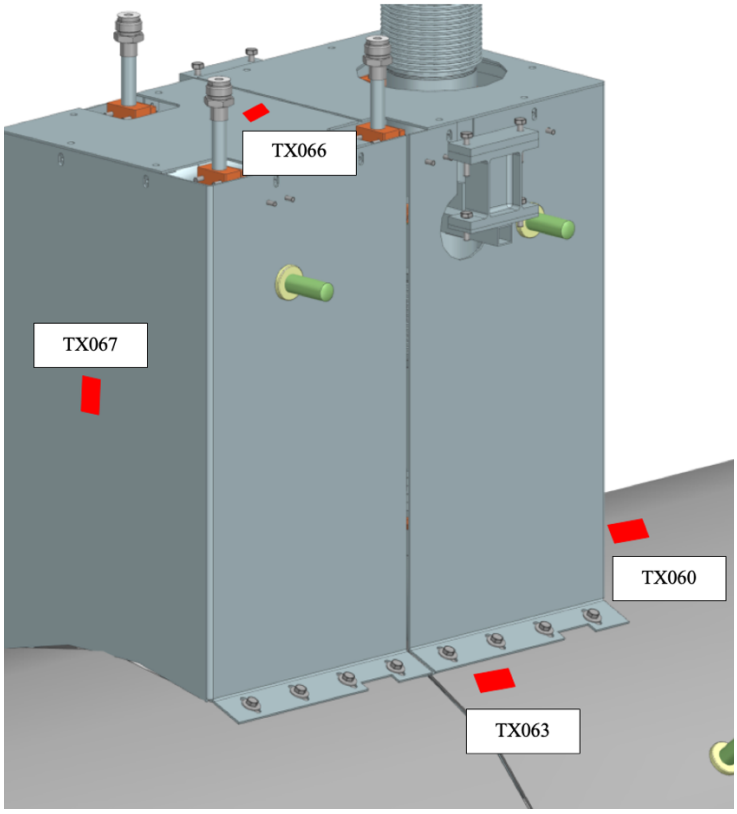

Figure 24: Position of the Temperature temperature sensors position on the edge and on the upper thermal shield.

To monitor the temperature of the upper thermal shield, three sensors were utilized: TX060 and TX063 in Fig. 25, and TX065 in Fig. 26. It is worth noting that the placement of these temperature sensors was not ideal for our specific purpose. As all the sensor locations were situated farthest from the heat sink (namely, the cooling pipe), the temperatures recorded by these sensors represent an upper bound value within the upper thermal shield.

Although the placement of the sensors may not have been optimal, they still provided valuable data regarding the upper thermal shield's temperature characteristics.

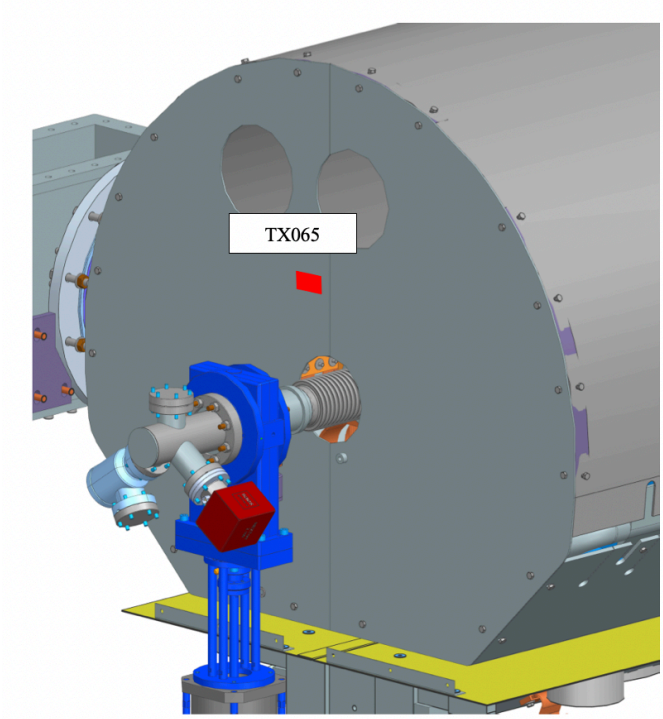

Figure 25: Position of the temperature sensors position on the edge and on the upper thermal shield.

To monitor the temperature of the couplers, two sensors were placed on the thermal intercepts (Fig.26). Despite their close proximity to each other, these sensors exhibited two distinct trends. Sensor TX271 provided insights into the thermal connection between the coupler and the High-Temperature Thermal Shield (HTTS), while sensor TX270 captured the thermal connection between the coupler and the Low Temperature Thermal Source (LTTS).

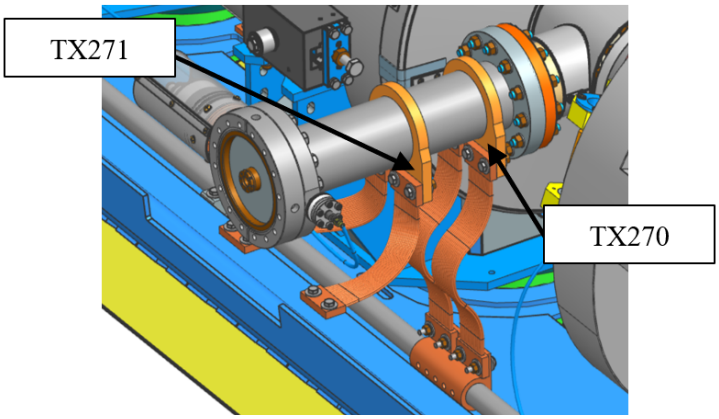

Figure 26: Position of the Temperature sensor positions on the coupler.

The temperature monitoring of the cold mass is facilitated by sensors strategically placed throughout the system (Fig.27). Sensor TX201 is located directly on the cavity, providing crucial data on its temperature dynamics. Additionally, sensors TX214 and TX514 are positioned on the support post, while sensors TX212 and TX512 are installed on the cavity support.

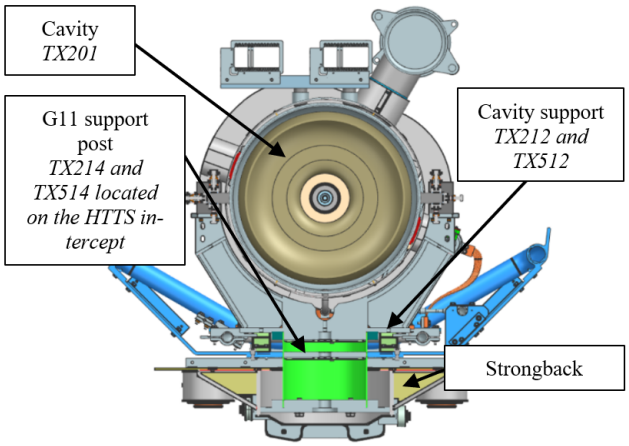

Figure 27: Position of the Temperature temperature sensorss positions on the beamline and strongback.

Fig. 28 illustrates the position of sensors along the relief line. It should be noted that the sensors are positioned at the warmest spots of the relief line. However, no sensors are placed at the end of the relief line which is directly connected to the 2K line, where the temperature is significantly colder. Therefore, the sensors provide again measurements of the relief line

temperatures at relatively warmer locations, while the coldest temperature at the end of the relief line is not directly monitored.

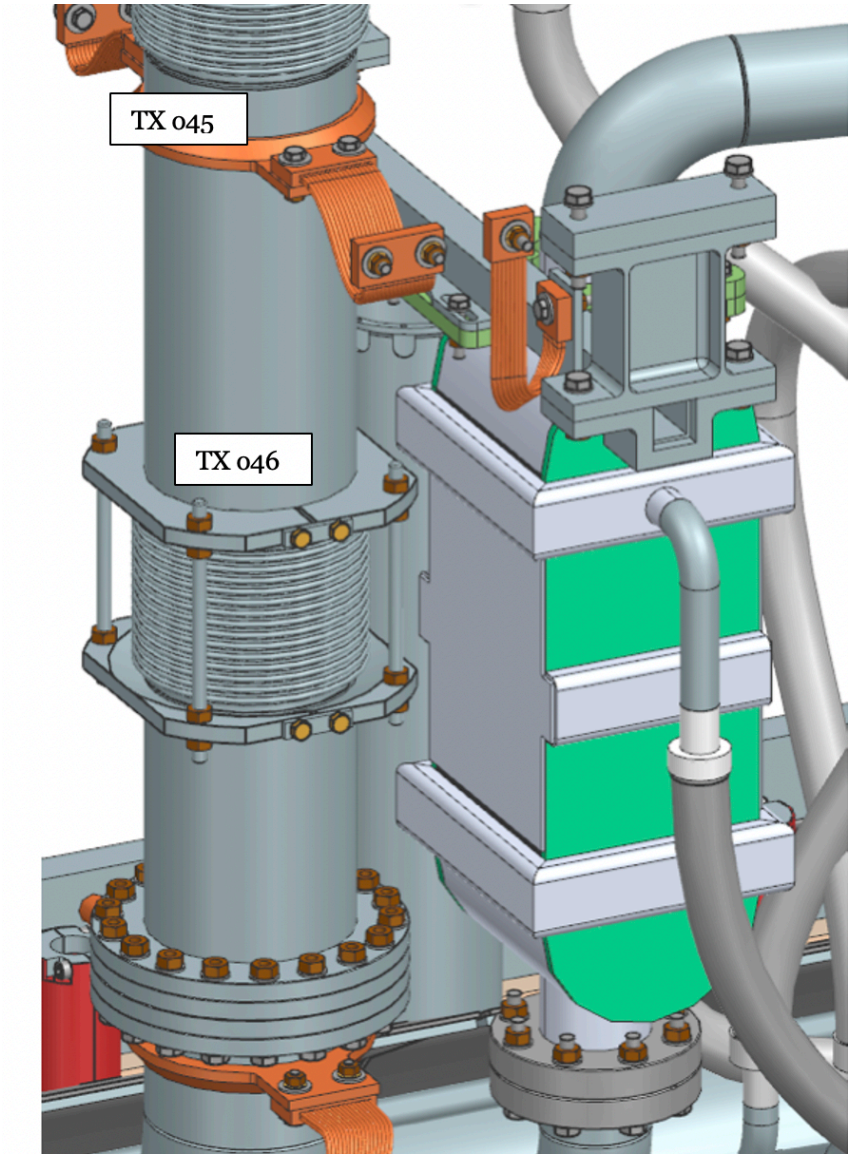

Figure 28: Position of the Temperature sensorss positions on the Relief Line.

4. Model

The heat load calculations in this study were performed using MATLAB/Simulink [9] a widely utilized software platform for system modeling and simulation. In Simulink, each component within the system was modeled as a thermal mass, taking into account its mass and thermal capacity. The model used in this study is therefore a lumped parameter model, where each component is treated as a single thermal mass with a uniform temperature. It is important to acknowledge that in reality, temperature gradients may exist within a mass or component due to geometrical features and local variations in heat transfer and thermal conductivity. However, for the purpose of simplification and computational efficiency, the lumped model assumes a single temperature value for the entire mass. The thermal connections between components were established based on reasonable assumptions and simplifications to ensure the model's simplicity. Connections with low heat transfer rates were considered negligible to streamline the analysis for example the radiation from vacuum vessel to the cavities via cryo-ports and via pressure transducer line (shown in Fig.6) due to the absence of the thermal shield in those ports.

The cooling process was simulated in three distinct steps, each corresponding to a different phase of the cooling process. The inlet temperature of the helium, employed for refrigeration purposes, served as the input parameter for the simulations. By incorporating these inputs and modeling the system components as thermal masses, the transient behavior of the heat loads could be accurately captured and analyzed.

In the modeling framework of the cryomodule, certain hypotheses were established to simplify the analysis and ensure a reasonable representation of the heat transfer phenomena. First, it was assumed that the contribution of heat transfer through convection within the cryomodule is relatively negligible due to the presence of a vacuum vessel that maintains a high vacuum for efficient thermal insulation. Another hypothesis made is that the assembly of the cavities, 2K line, and connections between cavities is considered as a single thermal

mass within the model. This is primarily due to the rapid cooling process, which occurs at such a fast rate that high thermal gradients are not observed within this assembly. Consequently, treating the cavities, 2K line, and connections as a unified thermal mass simplifies the analysis and modeling of heat transfer within this system. In the following subsections, the thermal masses, thermal resistances, and boundary conditions are described in detail.

4.1. Thermal Masses and Materials

In this chapter, the masses and materials used in the model are presented. Table 1 provides information on the masses for the single model component, although it should be noted that in certain cases, there may be multiple units for each component (Section 2). The parameters of the vacuum vessel are provided for the reader's curiosity, although they do not directly affect the model as the vacuum vessel is assumed to be at ambient temperature and therefore is not modeled as a component, but as a radiative boundary condition for the thermal shield. As for the support post, only the disk made of T6 aluminum is considered as a significant mass, while the G11 material has a negligible mass. Consequently, the G11 material is treated as a thermal resistance between the aluminum disk and the surrounding components, facilitating the heat transfer analysis.

For the couplers, considering the high thermal gradient within them, three masses have been taken into account. The first mass, depicted on the right side in Fig.29, represents the portion of the coupler that is exposed to ambient temperature as it lies outside the thermal shield. The second mass consists of the first section on the right side, which includes the 316 stainless steel pipe, and the copper intercept (indicated by the yellow ring), representing the High Temperature Thermal Shield (HTTS) intercept. The third mass encompasses the remaining part of the pipe and the additional copper intercept, representing the Low Temperature Thermal Shield (LTTS) intercept. By dividing the coupler into these distinct masses, the temperature variations and heat transfer within the coupler can be more accurately captured and analyzed.

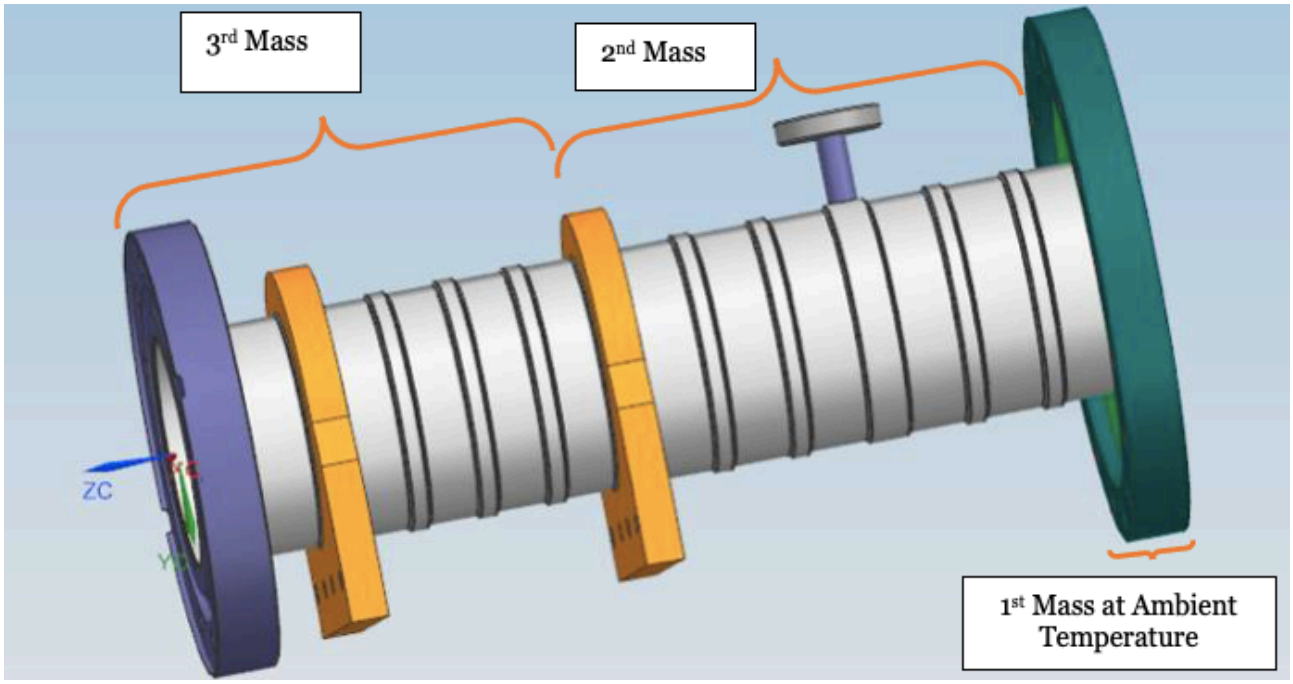

Figure 29: Model of the Coupler: definition of the different Masses.

A similar approach has been implemented for the relief line (Fig.30). It is divided into three masses to account for the distinct temperature gradients within the line. The first mass represents the portion of the relief line that is exposed to ambient temperature, as it is located outside the thermal shield. The third mass represents the part of the relief line inside the cavity. However, due to the presence of bellows connecting the first and third masses, which create a significant temperature gradient, a second mass is introduced. This second mass is connected to both the first and third masses and helps capture the temperature variations along the relief line more accurately.

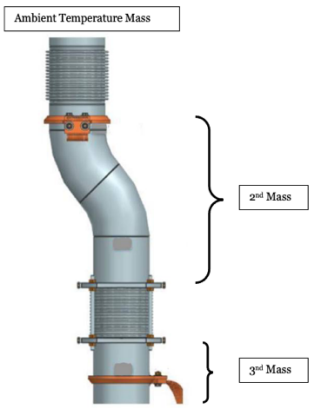

Figure 30: Model of the Relief Line: definition of the different masses.

Due to the convection cooling by the surrounding helium and the fact that the cavity is fully immersed in the helium, there are no significant temperature gradients within the cavity. Therefore, both the niobium part (cavity) and the titanium vessel have been considered as part of the same mass. This lumped mass approach allows for a simplified representation of the thermal behavior within the cavity, as the temperature is assumed to be uniform throughout the entire object.

Table 1: Materials and Masses of all components in the model.

Component	**Material**	**Mass (kg)**
Vacuum Vessel	A516 Steel	3482
Strongback	Al-6061	926
Support Post	T6 Aluminum	2.3
Cavity Support	Titanium	24
Lower Thermal Shield	Al 1100	160
Upper Thermal Shield	Al 1100	127.5
Side Thermal Shield	Al 1100	13.5
Edge Thermal Shield	Al 1100	6
Coupler First Mass	316 Stainless Steel	2
Coupler Second Mass	316 Stainless Steel, Copper	0.84
Coupler Third Mass	316 Stainless Steel, Copper	0.84
Relief Line First Mass	316 Stainless Steel,	1.3
Relief Line Second Mass	316 Stainless Steel,	1.3
Relief Line Third Mass	316 Stainless Steel,	6.5
Cavity	Titanium, Niobium	235

4.2. Thermal resistances

In this section, the thermal connections between the components are comprehensively explained, taking into account the two main modes of heat transfer involved: conduction and radiation. Convection, on the other hand, is primarily considered in the context of the refrigeration process between the helium and the flowing pipe. The parameters related to convection are specifically incorporated in a Simulink block, which will be further elucidated in subsequent sections. This block allows for a detailed analysis and modeling of the convective heat transfer occurring within the system. For the analysis of conduction, an analogy based on the electrical resistance concept is employed. This analogy is applicable in the special case of one-dimensional heat transfer with no internal energy generation and uniform material properties. The first hypothesis proves to be reasonable since there is not internal energy generation. However, the second hypothesis depends on the temperature gradient across the component being treated as a thermal resistance.

Just as electrical resistance is associated with the flow of electricity, thermal resistance is associated with the conduction of heat.

The concept of resistance is defined as the ratio of a driving potential to the corresponding transfer rate. Equation 1 shows the correlation between the thermal flow Q [W], the temperature gradient ΔT and the thermal resistance R_{th} [K/W]. Equation 2 shows the correlation between the electrical resistance R_{el} [Ohm], the current I and the voltage V [Volt].

$$\Delta T = R_{th} \cdot Q \quad \text{Equation 1}$$

$$V = R_{el} \cdot I \quad \text{Equation 2}$$

In the case of conduction in a plane wall, the thermal resistance can be described using Equation 3. [26]

$$R_{th} = \frac{L}{Area \cdot \lambda}$$ Equation 3

where L is the distance between the two materials involved in the heat transfer process [m], the area considered is the one of the object normal to the direction of heat transfer [m²], λ is the conductivity of the material between the two materials [W/(m·K)].

Similarly, in the context of electrical conduction within the same system, Ohm's law provides an electrical resistance described by Equation 4. By utilizing this analogy, the thermal behavior and conductive heat transfer in the system can be effectively analyzed and modeled.

$$R_{el} = \frac{L}{\sigma \cdot A}$$ Equation 4

where σ is the electrical conductivity [S/m]. Composite walls can exhibit series-parallel configurations, which introduce multidimensional heat flow characteristics. However, in many cases, it is reasonable to simplify the analysis by assuming one-dimensional conditions. In this approach, the composite wall can be represented as a complex thermal circuit, where the nodes correspond to the thermal masses, and the branches correspond to the thermal links.

In the context of this model, it is not realistic to assume that the material properties, such as conductivity, remain constant throughout the cryomodule, as the temperature ranges from 300K to 2K. To account for this variability, a "Variable Thermal Resistance" block is incorporated into the model. This block is designed to represent the conductive thermal resistances and is driven by a "1D Lookup Table" block (Fig.31). The lookup table stores the resistance values of the material as a function of temperature. During each iteration, the temperature of the component is calculated using a "Temperature Sensor" block (Fig.31), and the corresponding temperature value is passed to the 1D lookup table, which dynamically retrieves the corresponding resistance value. The values of thermal resistance in the 1D

Look Up Table are determined using Equation 3, where the thermal conductivity is considered as a function of temperature. In each mass considered in the model, there is a single temperature value, which consequently determines the thermal conductivity and, subsequently, the thermal resistance. Therefore, when considering components such as stripes or any other mass, the assumption of uniform material properties holds true only if the temperature gradients within that particular mass are small. The temperature dependence of the thermal conductivity for different materials can be found in the appendix. All the properties are taken from [27].

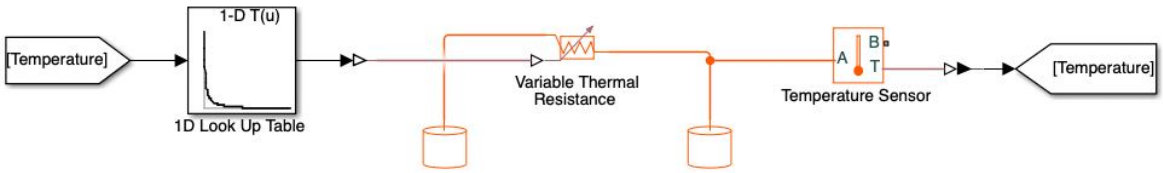

Figure 31: Variable Thermal Resistance and 1D Lookup Table and Temperature Sensor.

As opposed to the conductive heat transfer, the radiative heat transfer is not modeled as a thermal resistance in this simulation. Instead, a Simulink block called "Radiative Heat Transfer" is utilized (Fig.32). This block incorporates Equation 5, which requires the input of the emitting area and the heat transfer coefficient.

$$Q = k \cdot A \cdot \Delta T \quad \text{Equation 5}$$

To accurately account for radiative heat transfer, the heat transfer coefficients have been carefully evaluated for each specific case, considering the geometry and emissivities of all the materials involved in the cryomodule. Two methods have been employed to calculate the radiative heat transfer coefficient. The first method, described by equation 6, is applicable to parallel plates, while the second method, described by equation 7, is used for concentric cylinders. These equations [28]provide a means to determine the radiative heat transfer

coefficient (k) in each respective configuration, where ϵ_1 is the emissivity of the surface of the emitting component, ϵ_2 is the emissivity of the surface of the receiving component, r_1 and r_2 are the emitting and receiving cylinder radii, respectively, and finally σ is the Stefan Boltzmann constant $[W/m^2 \cdot K^4]$.

$$k = \frac{\sigma}{\left(\frac{1}{\epsilon_1}+\frac{1}{\epsilon_2}-1\right)} \qquad \text{Equation 6}$$

$$k = \frac{\sigma}{\left(\frac{1}{\epsilon_1}+\frac{1-\epsilon_2 r_1}{\epsilon_2\ r_2}\right)} \qquad \text{Equation 7}$$

Figure 32: Model of the Radiative Heat Transfer in Simulink environment.

The convection heat transfer is specifically utilized in the refrigeration sections of the model (Fig.33), employing the liquid library in Simscape. The primary block used in this context is the pipe block, which represents a segment of the pipeline containing a fixed volume of liquid. Within the pipe, the Nusselt number correlations determine the heat exchange coefficient that describe the heat transfer between the helium flowing inside and the walls of the pipe.

Preceding the pipe block in Fig.33 there are two additional blocks. The first is a controlled mass flow rate source, where the mass flow is inputted. During the cooling process, the mass flow experiences two distinct values: 29 g/s for the first two hours, followed by 27 g/s for the remainder of the cooling period. This is achieved using a step function. The second block is

the controlled reservoir, responsible for defining the temperature of the inlet helium. The subsystem shown in Fig. 33 is the boundary condition of the helium inlet temperature. Connected to the pipe block, still in Fig.33, there is the "Thermal Liquid Setting" block, where the properties such as density, viscosity, and thermal conductivity of the helium are specified as inputs. The functional dependencies of these properties for helium can be found in the Appendix. Finally, on the right side, there is a reservoir block that represents the sink temperature where the helium ends, with ambient temperature being selected for this purpose.

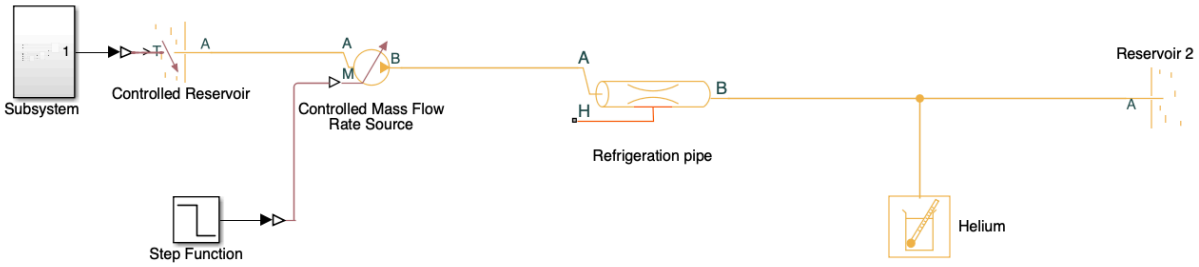

Figure 33: Model of the pipe used for the refrigeration of the System.

4.2.1. HTTS, LTTS and Cavities Thermal Connections

Given the complexity of the model, a systematic strategy was employed to elucidate the thermal connections among the components. The approach involved analyzing the heat loads one at time, starting with that on the cavity (comprising the 2K line and the cavity itself, as explained in section 2.7), followed by the LTTS, and concluding with the HTTS. This sequential analysis allowed for a detailed examination of the heat transfer processes within each subsystem, facilitating a comprehensive understanding of the overall thermal behavior of the system. In Fig. 34 the cavity's heat exchanges are shown, commencing with the radiative heat loads on the cavity, the primary heat exchange occurs between the cavity and the thermal shield. By the end of the cooling process, the thermal shield significantly attains a higher temperature. Furthermore, heat is also exchanged between the cavity and the cavity

supports, which are also at slightly higher temperatures. Table 2 shows all the parameters considered for the evaluation of radiative heat transfer. Regarding conductive heat transfer, the cavity exchanges heat with the coupler through a stainless steel pipe. The relief line terminates directly in the 2K line, thus the resistance at the junction of the two 316 stainless steel pipes has been considered (Fig.15). On the left side, resistances associated with instrumentation, such as RF cables, tuners, and PT lines, are present. These wires establish connections between the cavity and warmer sources such as the LTTS, or HTTS, and despite their high resistances, they contribute to heat transfer in some manner. The cavity exchange heat with the boundary condition of vacuum vessel via the heater wires. The figure depicts a representative resistance for graphical clarity, but it is important to note that multiple resistances may exist in parallel in certain cases. Table 3 provides information on the number of conductive thermal resistances in parallel, their respective lengths and areas, and the materials of the components involved in heat exchange with the cavity. The subsystems for the coupler and relief line are depicted in Section 4.4.2, providing a detailed representation of their respective components and interactions.

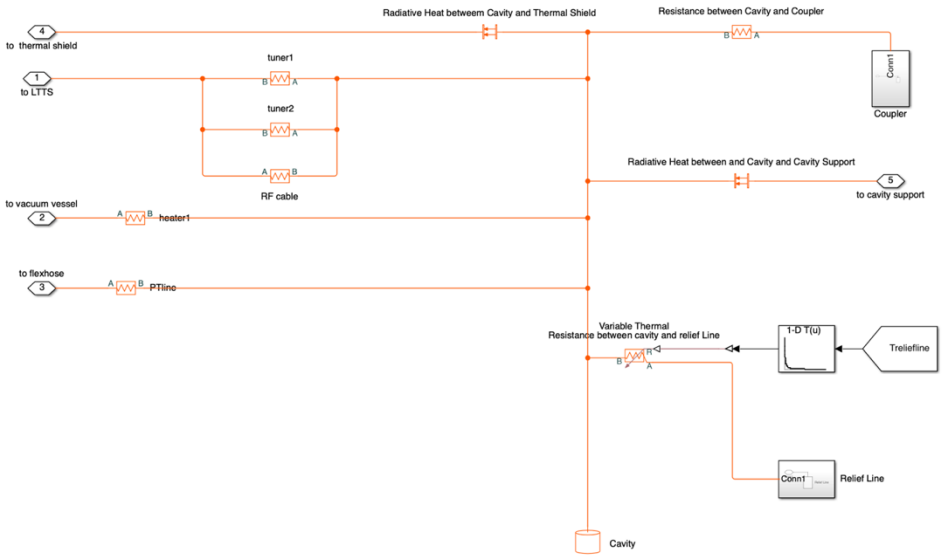

Figure 34: Model of the thermal Connections between the Cavity and the Surrounding Components.

Table 2: Radiative Heat Transfer Parameters on the Cavity.

Emitting Component	Emissivity Emitting Component	Emissivity Receiving Component	Heat Transfer Coefficient
Thermal Shield	0.7	0.09	4.6e-09
Cavity Support	0.9	0.5	6.5e-08

Table 3: Conductive Heat Transfer Parameters on Cavity.

Component	Material	Length (m)	Area (m^2)	Number of Resistances in Parallel
Coupler	Steel	0.023	3,9e-04	1
Coupler	Copper	0.023	2.3e-6	1
RF Cable	Copper	0.5	6.6e-7	12
Tuner	Copper	1.2	8.1e-8	48
PT line	Copper	1.2	8.1e-8	160
PT line 2	Copper	1.2	5.2e-7	4
Relief Line	Steel	60e-3	5.1e-4	1
Flex hoses	Copper	1.2	8w-8	180

Fig. 35 illustrates the thermal connections involving the LTTS and its interaction with other components. Radiative heat exchange is not accounted for in the LTTS connections. This is due to the fact that the LTTS does not experience a significant temperature difference compared to the surrounding components, making the contribution of radiative heat transfer negligible. The left side of the figure shows the thermal resistances, represented as thermal straps, between the LTTS and the cavity supports, as well as between the LTTS and the Couplers. These connections facilitate the transfer of heat between the LTTS and the corresponding components. On the right side of the figure, similar to the cavity, the wires and cables of the instrumentation are considered as potential sources of heat and between the

relief line and LTTS the resistance at the junction of the two 316 stainless steel pipes has been considered. These elements contribute to the overall thermal dynamics of the system by introducing additional heat loads to the LTTS. The LTTS exchange heat with the boundary condition vacuum vessel via two different types of tuner wires in parallel. Table 4 provides information on the number of resistances in parallel, their respective lengths and areas, and the materials of the components involved in heat exchange with the cavity.

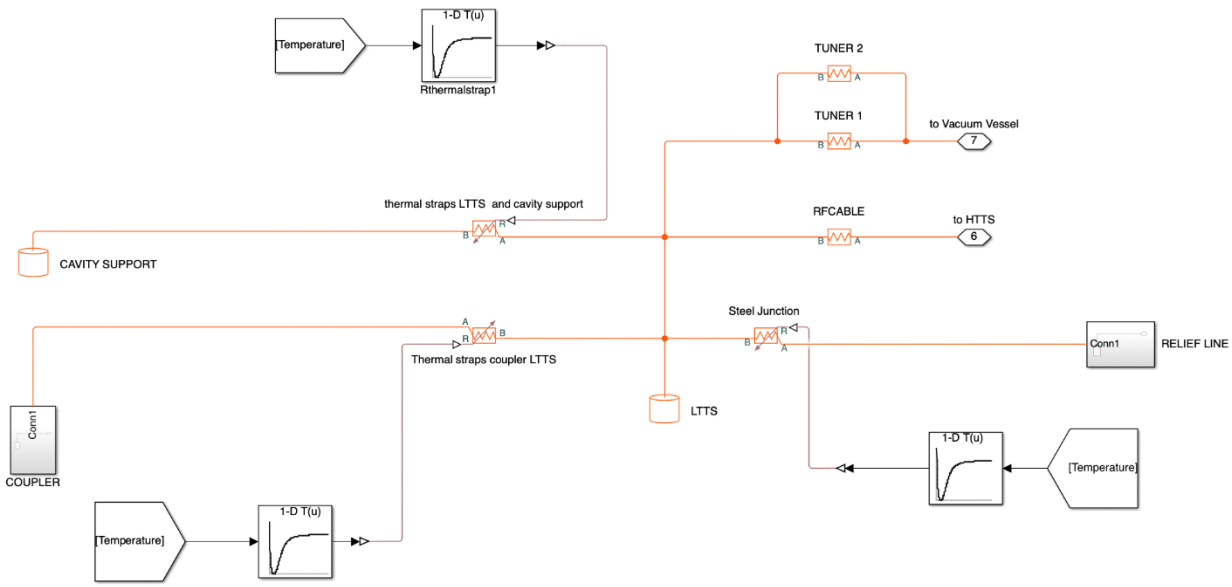

Figure 35: Model of the thermal Connection between LTTS and Surroundings Components.

Table 4: Conductive Heat Transfer Parameters on LTTS.

Component	**Material**	**Length**	**Area**	**Number of Resistances in Parallel**
Coupler	Steel	0.082	3,9e-04	1
Coupler	Copper	0.082	2.3e-6	1
RF Cable	Copper	0.5	6.6e-7	12
Support Post	G10	0.03	1.9e-3	12

The thermal resistance around the HTTS (High-Temperature Thermal Shield) plays a crucial role in the heat transfer process (Fig.36). The dominant source of heat is the radiation from the vacuum vessel to the thermal shield. However, there are also additional heat losses from the relief line, flex hoses, couplers, and support posts, as these components are at higher temperatures compared to the HTTS line. Furthermore, the instrumentation connected to the vacuum vessel also contributes to some heat generation.

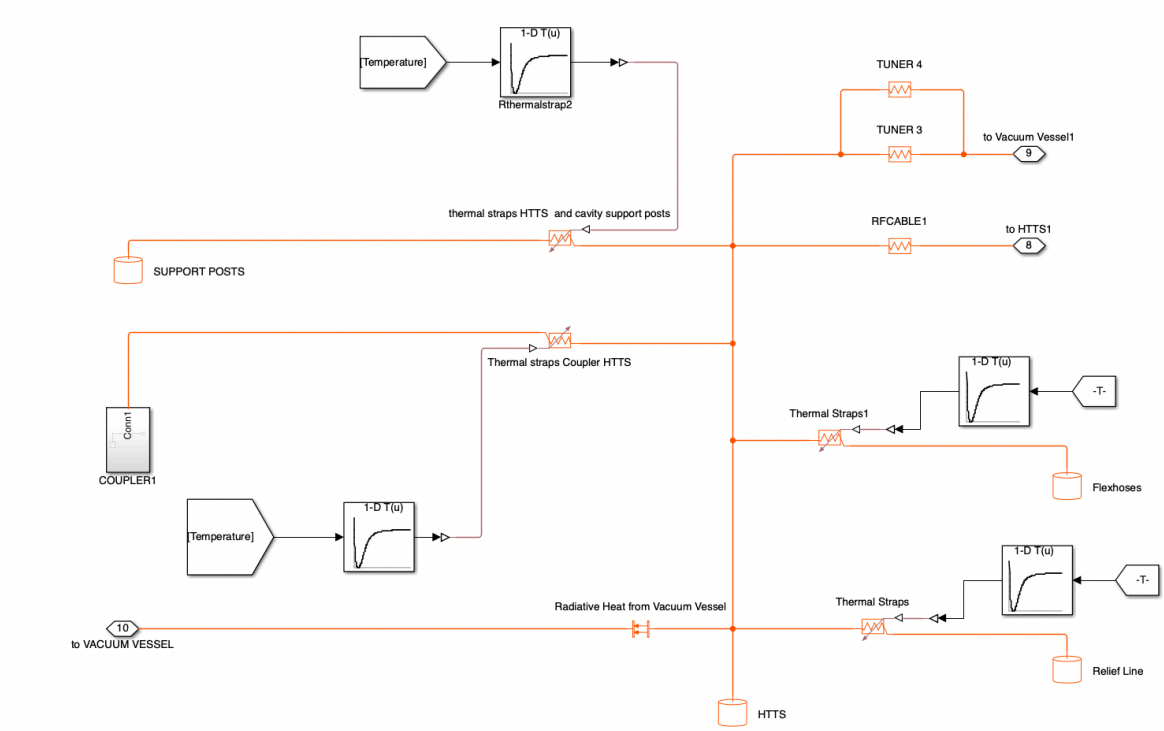

Figure 36: Model of the Tthermal Connection between HTTS and Surroundings Components.

Table 5 shows all the parameters considered for the evaluation of radiative heat transfer with vacuum vessel, since the heat transfer is with vacuum vessel this is also a boundary condition.

Table 5: Radiative Heat Transfer Parameters on the HTTS.

Emitting Component	**Emissivity Emitting Component**	**Emissivity Receiving Component**	**Heat Transfer Coefficient**
Vacuum Vessel	0.5	0.004	2e-10

Table 6 provides information on the number of conductive resistances in parallel, their respective lengths and areas, and the materials of the components involved in heat exchange with the cavity. The HTTS exchange heat with the boundary condition vacuum vessel via two different types of tuner wires in parallel.

Table 6: Conductive Heat Transfer Parameters on HTTS.

Component	Material	Length	Area	Number of Resistances in Parallel
Coupler	Steel	0.141	3,9e-04	1
Coupler	Copper	0.141	2.3e-6	1
RF Cable	Copper	0.5	6.6e-7	12

4.2.2. Internal Resistances to Couplers and Relief line

The thermal masses involved in Fig.37 are explained in Section 4.1. The thermal connections between the three masses within the coupler is established through a stainless-steel pipe with an inner layer of copper. To simulate this configuration, the pipe was modeled as having two parallel resistances, one representing the thermal resistance of the steel and the other representing the thermal resistance of the copper. The internal resistances within the masses of the relief line play a crucial role in modeling the heat transfer within this component. As discussed in Section 4.1, the relief line has been divided into three distinct masses due to the significant temperature gradient observed between each pair of them. To account for the thermal connections between these masses in the model, bellows are modelled by variable resistances (Fig.38). These bellows accommodate the movements and thermal contractions of the relief line, allowing for the transfer of heat between the different masses. Furthermore, the relief line is also thermally connected to the LTTS, the HTTS, and the cavity. These connections introduce additional resistances that influence the heat transfer between the relief line and these neighboring components. Accurately representing these internal resistances

is crucial for capturing the heat flow dynamics and ensuring a comprehensive model of the relief line's thermal behavior.

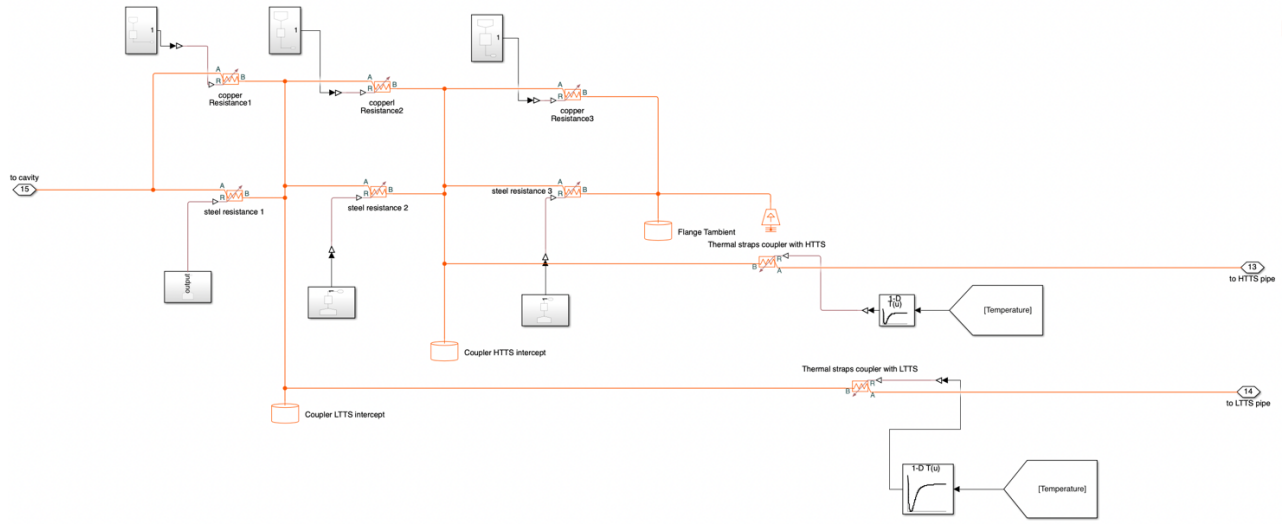

Figure 37: Model of the internal Resistances within the couplers.

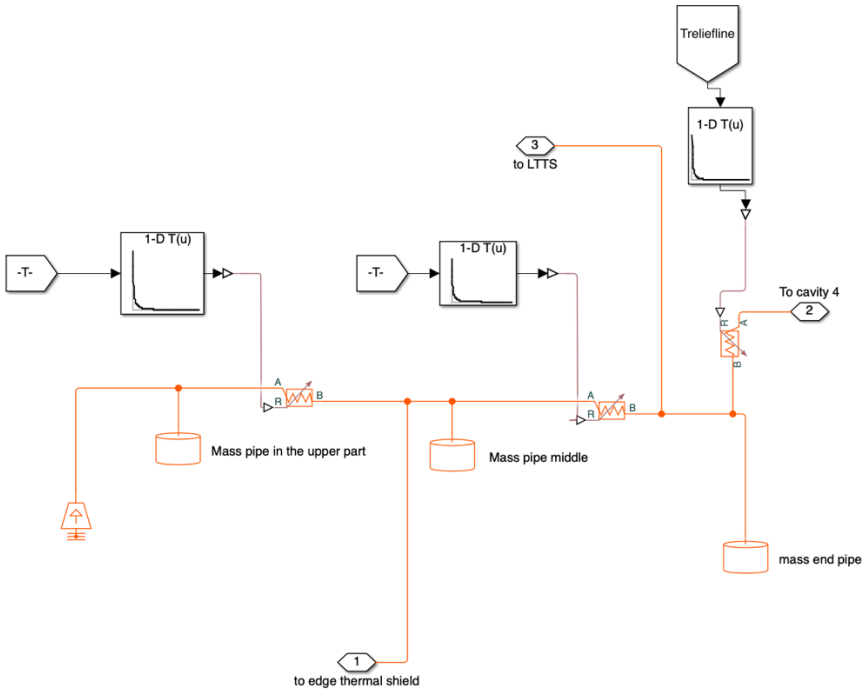

Figure 38: Model of the internal Resistances within the Relief Line.

4.3. Simulation setup: boundary conditions and driver

In the modeling of the cryomodule, certain boundary conditions were imposed to simulate the transient behavior of the system. The vacuum vessel, although its internal temperature

could be lower, was considered to be at ambient temperature throughout the entire transient simulation. This assumption was made due to the lack of precise temperature data within the vacuum vessel and as a simplifying approximation. However, it is important to note that the actual temperature inside the vacuum vessel may be lower than the ambient temperature due to the fact that it faces a cryogenic environment (the thermal shield). Furthermore, the inlet temperature of the pipe used for refrigerating the thermal shield was provided as an input to the simulation. It is important to note that as a hypothesis in the model, every point of the pipe used for refrigerating the thermal shield is considered to be at the same temperature as the inlet temperature. The function used to simulate the inlet temperature, as described in the cooling procedure of Fermilab, was constructed using Simulink's Switchers blocks. The function itself can be observed in Fig. 39, starting from the lower portion of the figure it can be seen that for the initial 21600 s (6 h), denoted as f(u), a ramp function is employed. This ramp function begins with an initial value of 260 K and has a slope of -0.003 K/s. Following this period, the function becomes a horizontal line at 200 K. After 7200 s (2 h), another ramp function is introduced, this time with a slope of -0.0036 K/s. Finally, after 108000 s (30 h), the function transits to another horizontal line at 70 K. This temperature boundary condition (Fig.40) is essential for accurately model the cool-down and assessing the thermal performance of the cryomodule during the transient process because every component connected to the pipe experiences the same inlet temperature regardless of the specific point of connection. As a result, each component is subjected to a heat transfer boundary condition with a mass at inlet temperature, assuming a uniform temperature distribution along the pipe.

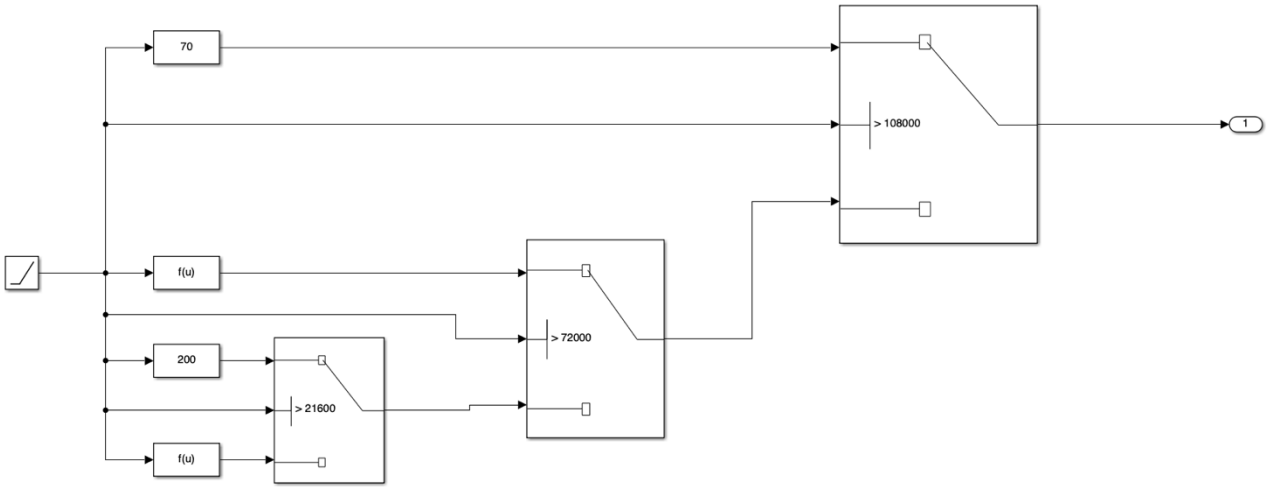

Figure 39: Implementation in Simulink of the Inlet Temperature evolution.

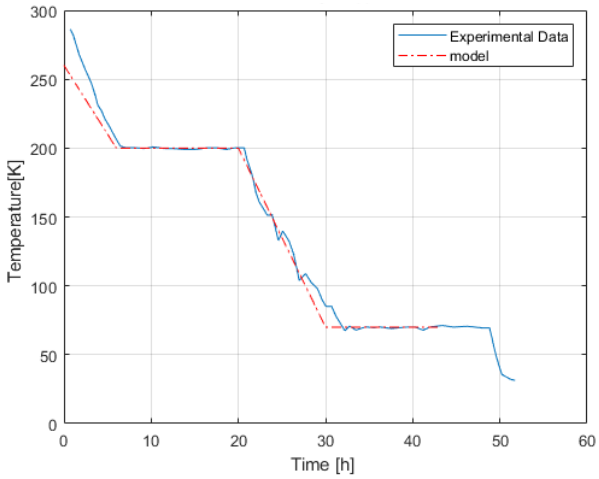

Figure 40: Inlet Helium Temperature.

The inlet temperature is employed to simulate the temperature cooldown of the thermal shield in the model. Unfortunately, due to a lack of sufficient data, as mentioned previously in Section 3.1, it was not possible to validate the second and third cooldowns. Therefore, the focus of the validation process was solely on the first cooldown, where temperature measurements were available. Table 7 provides a summary of the boundary conditions discussed in the preceding subsections. These boundary conditions define the external factors and parameters that influence the heat transfer within the system.

Table 7: Boundary Conditions.

Component	**Boundary Condition**
Coupler	Conduction with mass at ambient temperature
Relief Line	Conduction with mass at ambient temperature
Cavity	Conduction via Heater to Vacuum Vessel
LTTS	Conduction via Tuner to Vacuum Vessel
HTTS	Radiation with Vacuum Vessel
HTTS	Conduction via Tuner to Vacuum Vessel
HTTS	Conduction via Finger Welds to the Extruded Pipe

4.4. Global model of the cryomodule

In Fig.41 all the masses and all the thermal resistances are shown.

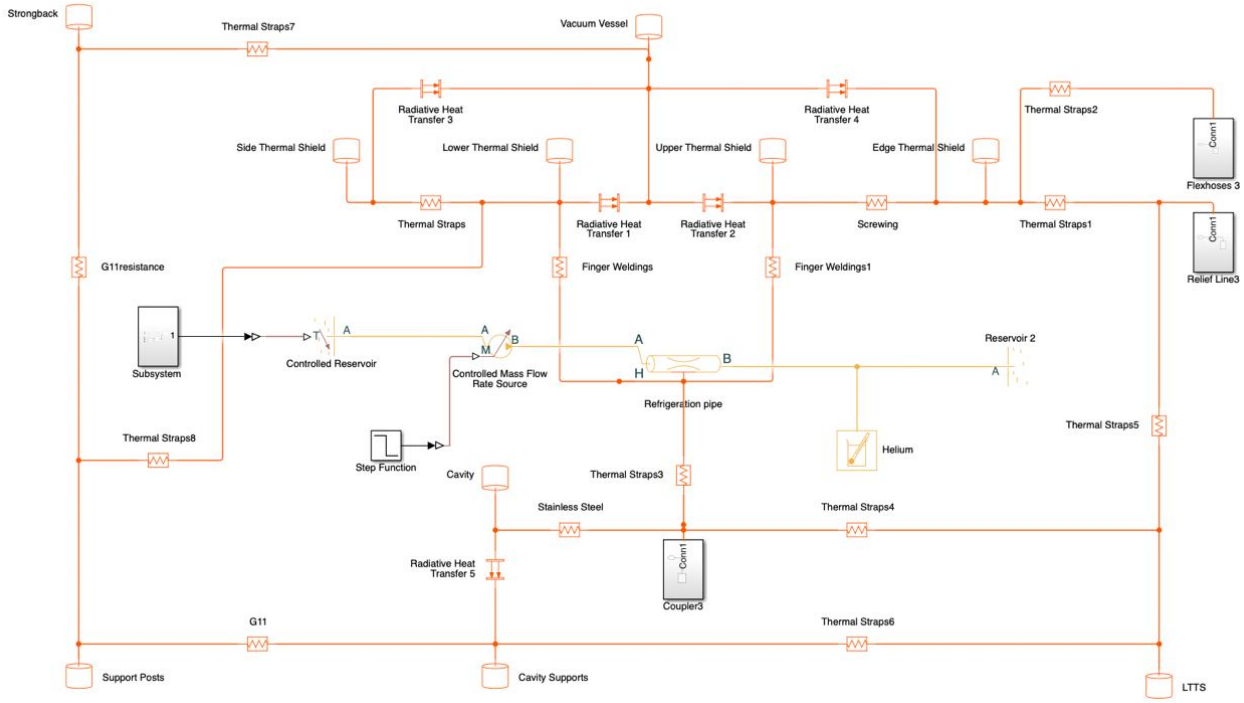

Figure 41: Global Resistances of the Cryomodule.

5. Results

This chapter presents the results of the study, which are divided into two main subchapters. The first subchapter focuses on the validation of the developed model, where comparisons are made between the simulated results and experimental data to assess the accuracy and reliability of the model. This validation process ensures that the model adequately captures the behavior and characteristics of the system under investigation.

The second subchapter delves into the primary objective of the thesis, which is to evaluate the heat loads at the steady state at the end of the cooling process. This analysis provides valuable insights into the distribution and magnitude of heat transfer within the cryomodule. By examining the heat loads of different components, such as the cavities, thermal shields, couplers, and support structures, a comprehensive understanding of the thermal behavior and performance of the cryomodule is obtained. The results obtained in this subchapter contribute to enhancing the overall knowledge and optimization of the Fermilab cryogenic system.

5.1. Model Validation

The primary objective of this model is not to predict component temperature during transient states, as finite element analysis (FEA) excel in that regard. Instead, the model serves to calculate the heat loads of each component, while the comparison between the model and experimental data verifies if these heat loads have been adequately considered. Transient states are not the main focus of this model as they are better analyzed by FEA. The 0D Simulink/Simscape model does not fully capture the complex temperature variations of each component. Nevertheless, by comparing the model to the experimental data under steady-state conditions, it becomes clear if the heat loads on the components have been properly accounted for.

5.1.1. Lower Thermal Shield

The results obtained for the lower thermal shield, in the first part of the cooling, are shown in Fig. 42. Results from the model match the experimental data within 6% on average (3% if considering only the more interesting steady state intervals). The slight discrepancies can be attributed to the fact that the model uses an average temperature of the lower thermal shield. The sensors used for the comparison are instead the ones shown in section 3.1, measuring on average a higher temperature.

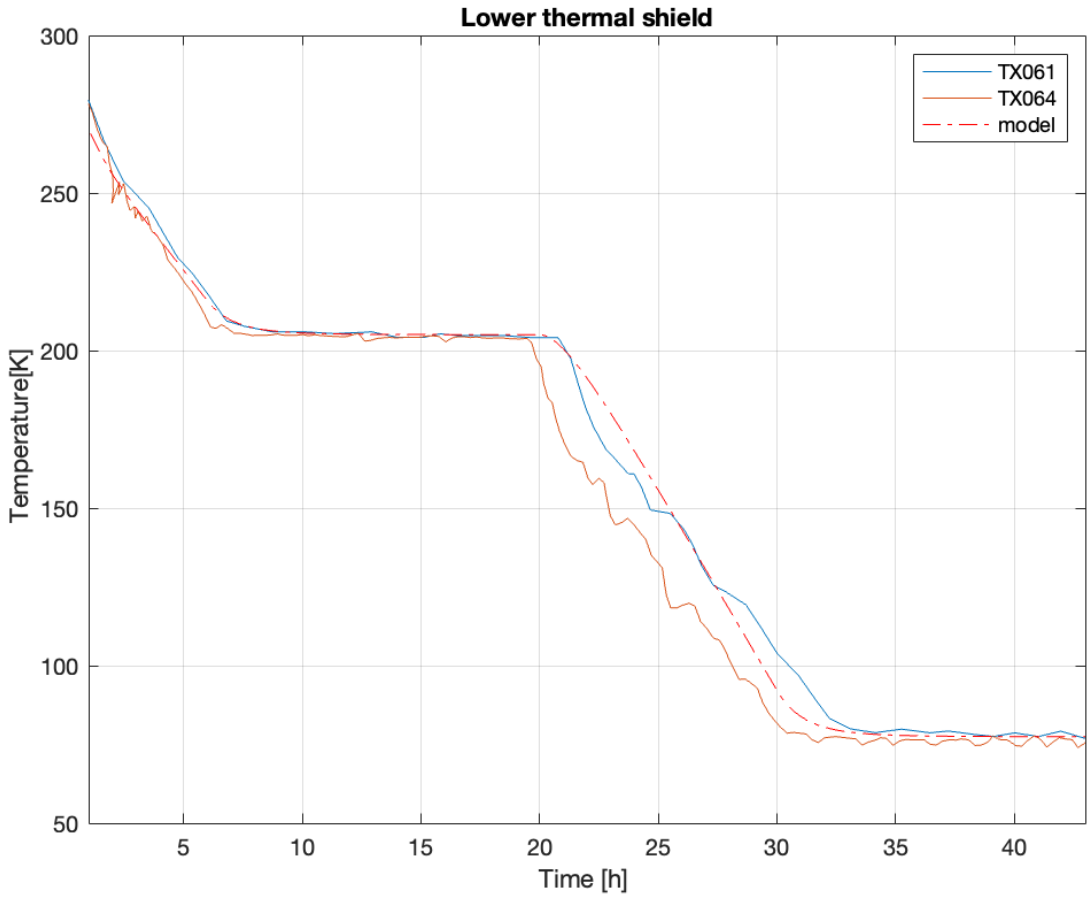

Figure 42: Validation results: of Lower Thermal Shield in the First Part of the Cool-down.

5.1.2. Upper Thermal Shield

The results obtained for the upper thermal shield are shown in Fig. 43. Results from the model match the experimental data within 10% on average (6% if considering only the more

interesting steady state intervals).. The slight discrepancy observed in the results of the upper thermal shield can be attributed to the positioning of the temperature sensors, measuring an upper bound of the upper thermal shield temperature range (see Section 3.1). It should be noted that the sensors used for monitoring are located in the warmest regions of the upper thermal shield. As a result, these measurements may not be entirely representative of the average temperature throughout the entire upper thermal shield.

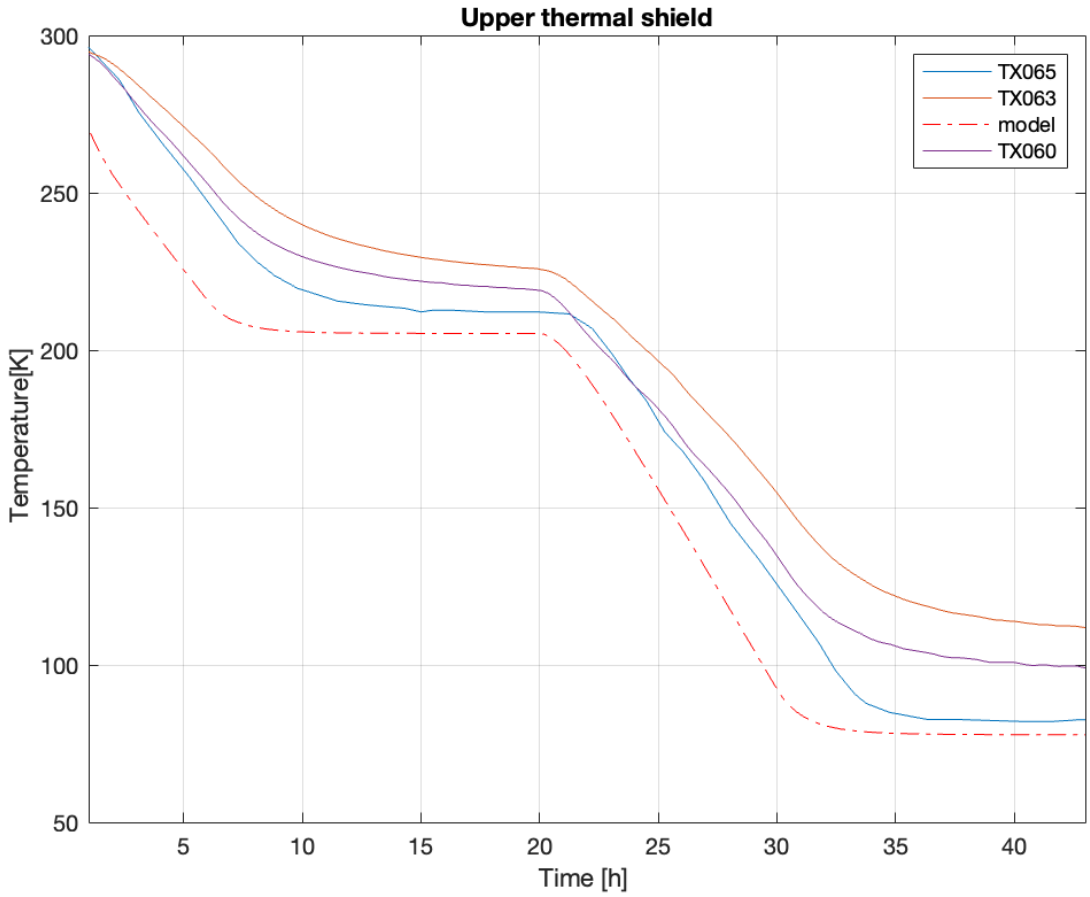

Figure 43: Validation of Upper Thermal Shield in the First Part of Cool-Down.

5.1.3. Edge Thermal Shield

The results obtained for the edge thermal shield are shown in Fig. 44. In the analysis of the edge thermal shield, it is observed that there is not a strong correlation between the model predictions and the experimental data: within 11% on average (8% if considering only the more interesting steady state intervals). This discrepancy suggests the presence of additional

heat losses from radiation that have not been accounted for in the model. The edge thermal shield, being in close proximity to other components and the surrounding environment, is susceptible to radiative heat transfer. Consequently, the model's inability to accurately capture these radiative losses may contribute to the observed mismatch between the model predictions and experimental data for the edge thermal shield. Future studies should focus on refining the model to incorporate the influence of other radiative heat losses and improve the matching of the edge thermal shield's behavior.

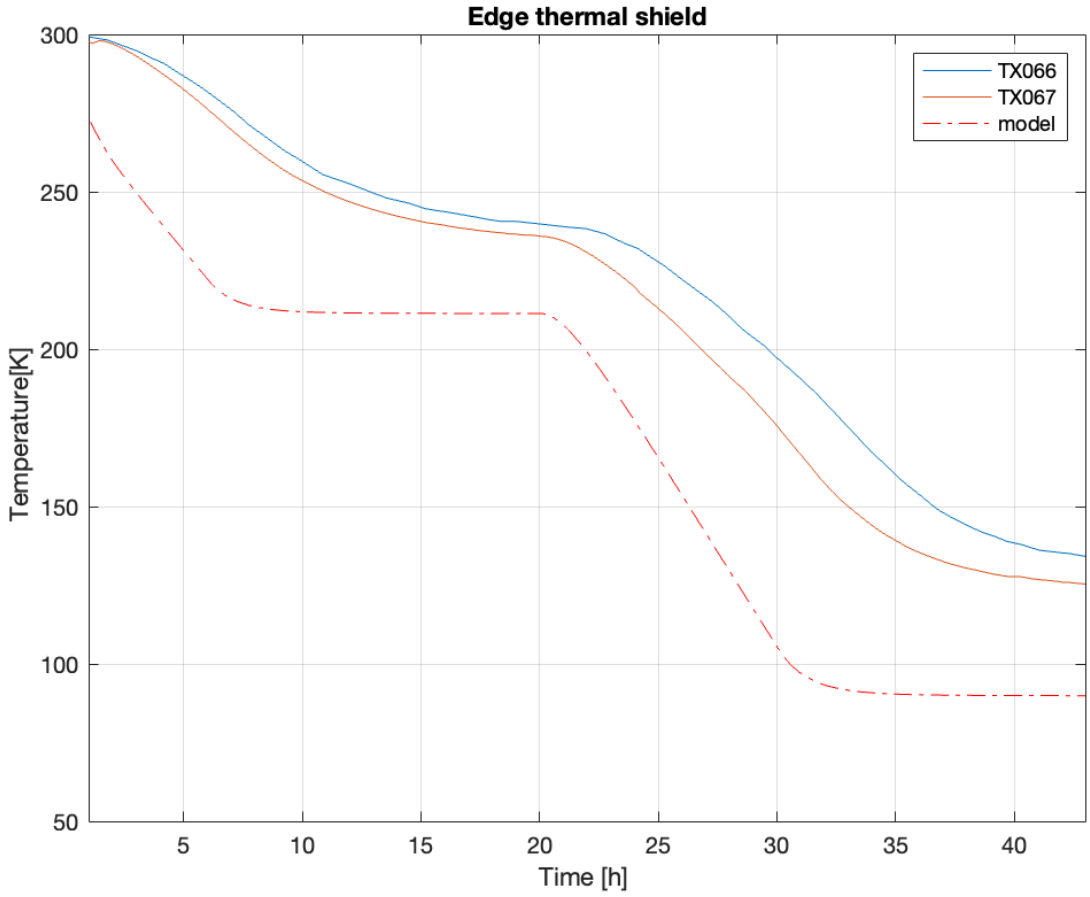

Figure 44: Validation of Edge Thermal Shield in the First Part of Cool-Down.

5.1.4.Side Thermal Shield

The side thermal shield does not reach a steady state within the simulated timeframe (Fig.45), making it difficult to establish a definitive evaluation of its performance. The temperature obtained from the model is slightly lower than the recorded data within 12% on

average (6% if considering only the more interesting steady state intervals), which could be attributed to the presence of internal bayonets within this component. These bayonets potentially contribute to radiation heat transfer towards the thermal shield. However, the consideration of this radiation contribution poses challenges due to the complexity of estimating accurate view factors, particularly given the extensive presence of pipes within the system.

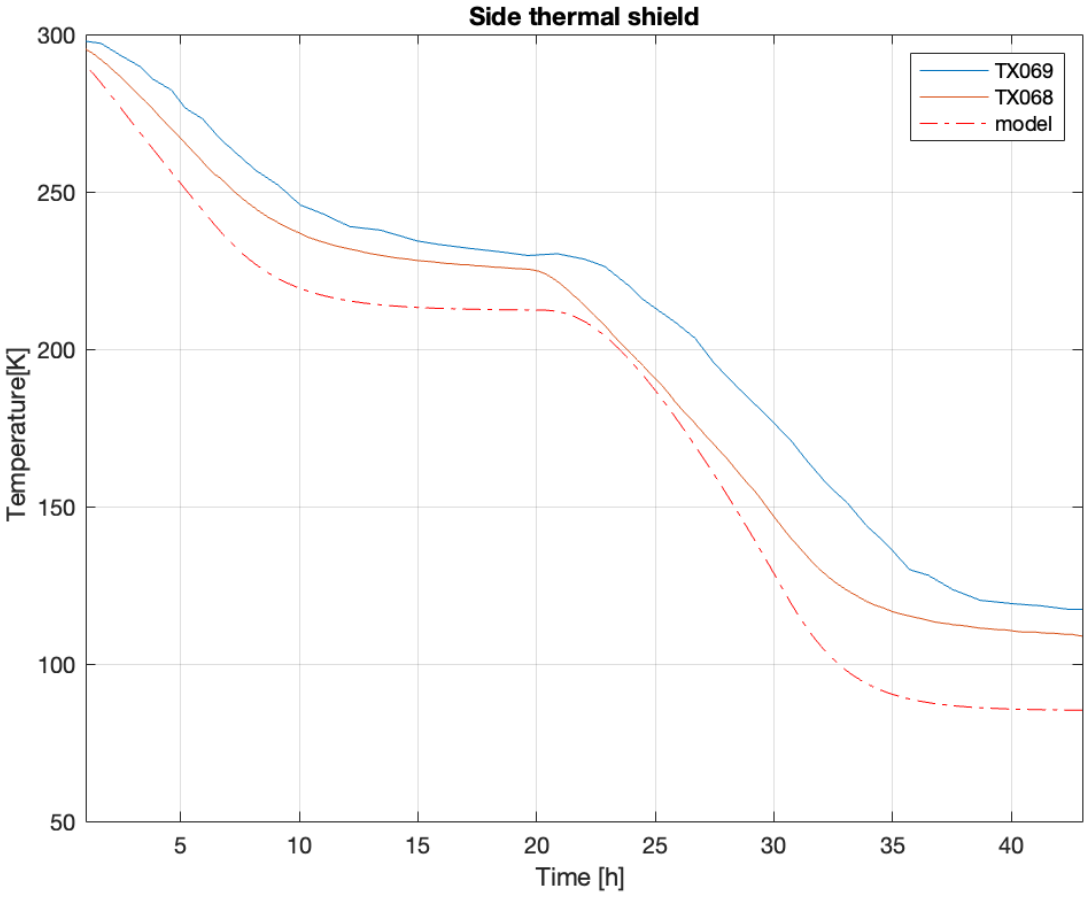

Figure 45: Validation of Side Thermal Shield in the First Part of Cool-Down.

5.1.5. Couplers

The observed discrepancy in Fig.46 between the model and the actual data within 3% on average (3% if considering only the more interesting steady state intervals) can be attributed to the complex structure of the couplers, which add challenges to estimate accurately the heat transfers. Additionally, the significant temperature difference between the two intercepts further contributes to the discrepancy between the model and the experimental data.

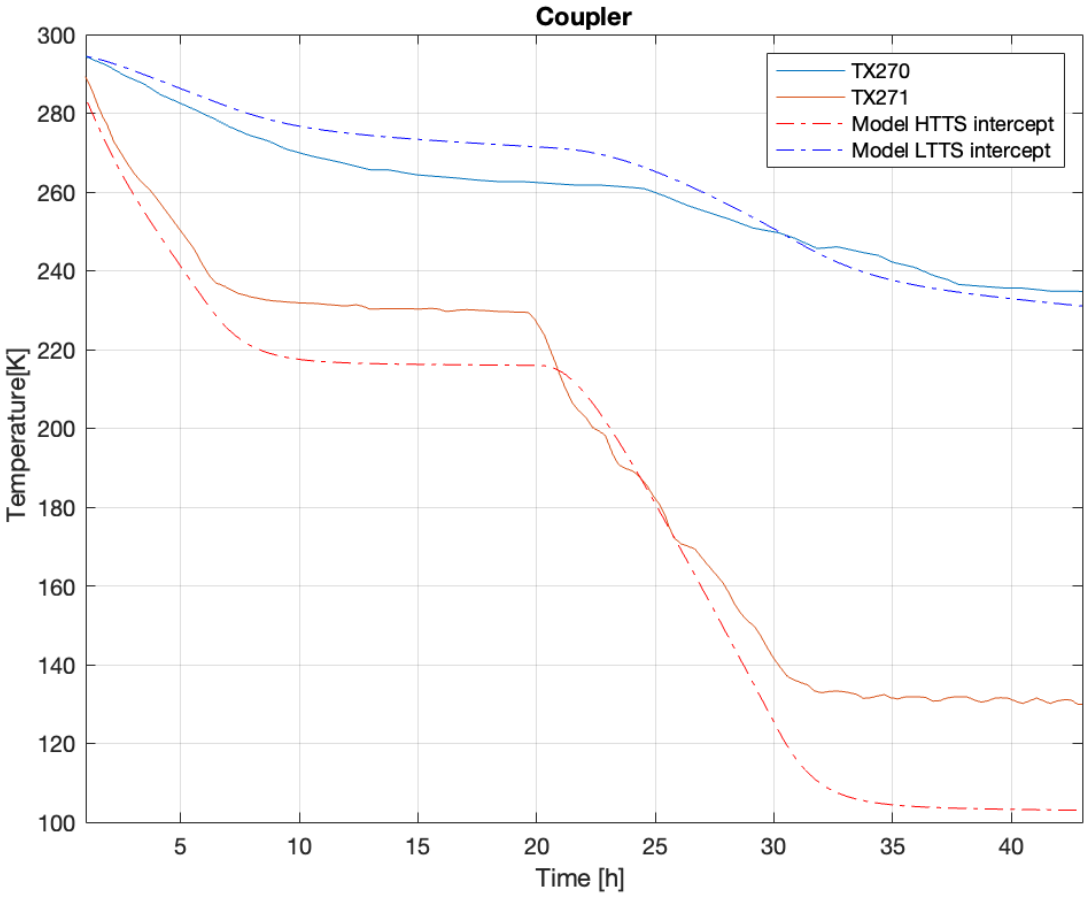

Figure 46: Validation of Couplers in the First Part of Cool-Down.

5.1.6. Cavity Supports

The results obtained for the cavity supports are shown in Fig. 47. The observed discrepancy of 10K in the temperature measurements can be attributed to the omission of thermal connections through mechanical interfaces. In the model, the connection between the relief line and the colder source (cavity) was considered solely based on radiative heat transfer. However, it is important to note that there are additional mechanical connections, such as screwing, which contribute to the thermal linking between the relief line and the cavity. The absence of these mechanical connections in the model likely accounts for the observed temperature discrepancy, which is 2%.

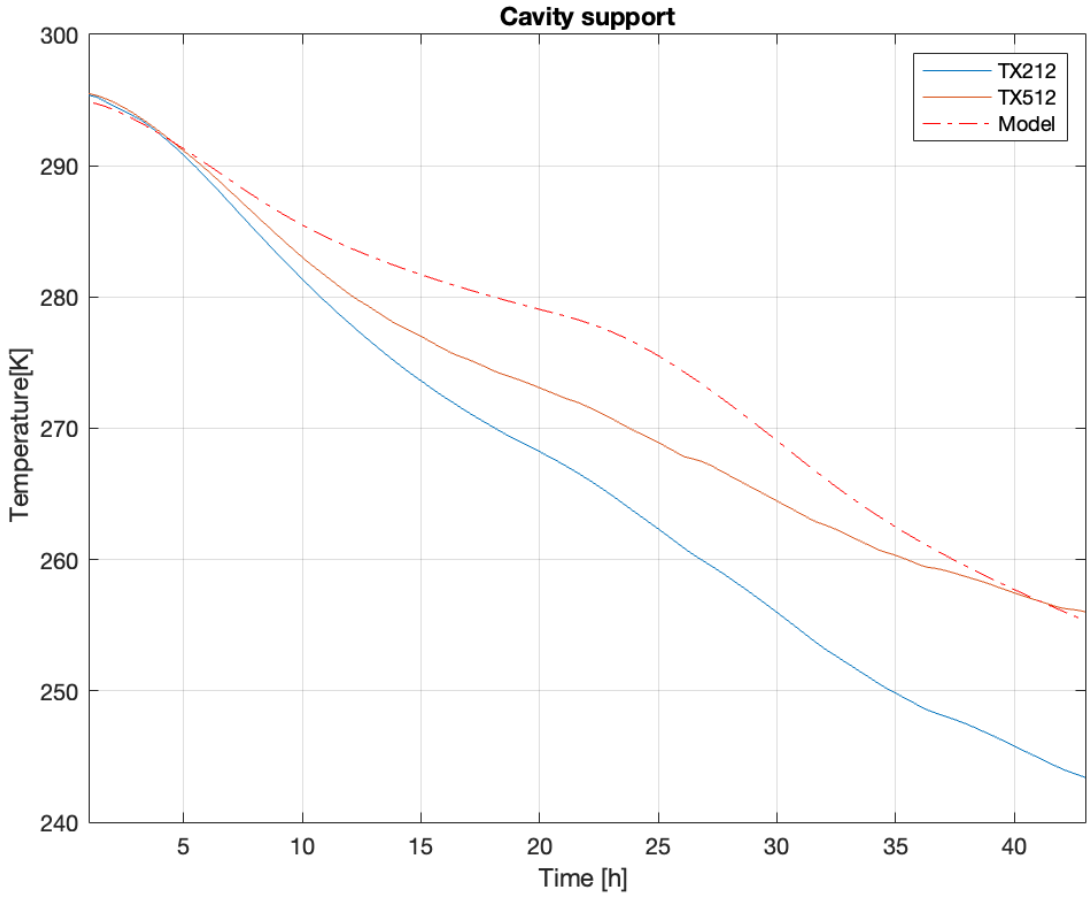

Figure 47: Validation of Cavity Supports in the First Part of Cool-Down.

5.1.7. Support Posts

Fig. 48 presents the results obtained for the support post disk during the initial phase of the cooling process. The plotted data demonstrates a close agreement with the measurements collected from the sensors, particularly in the evaluation of the steady-state conditions: within 5% on average (2% if considering only the more interesting steady state intervals). The model successfully captures the thermal behavior of the support post disk, effectively replicating the temperature trends observed in the experimental data.

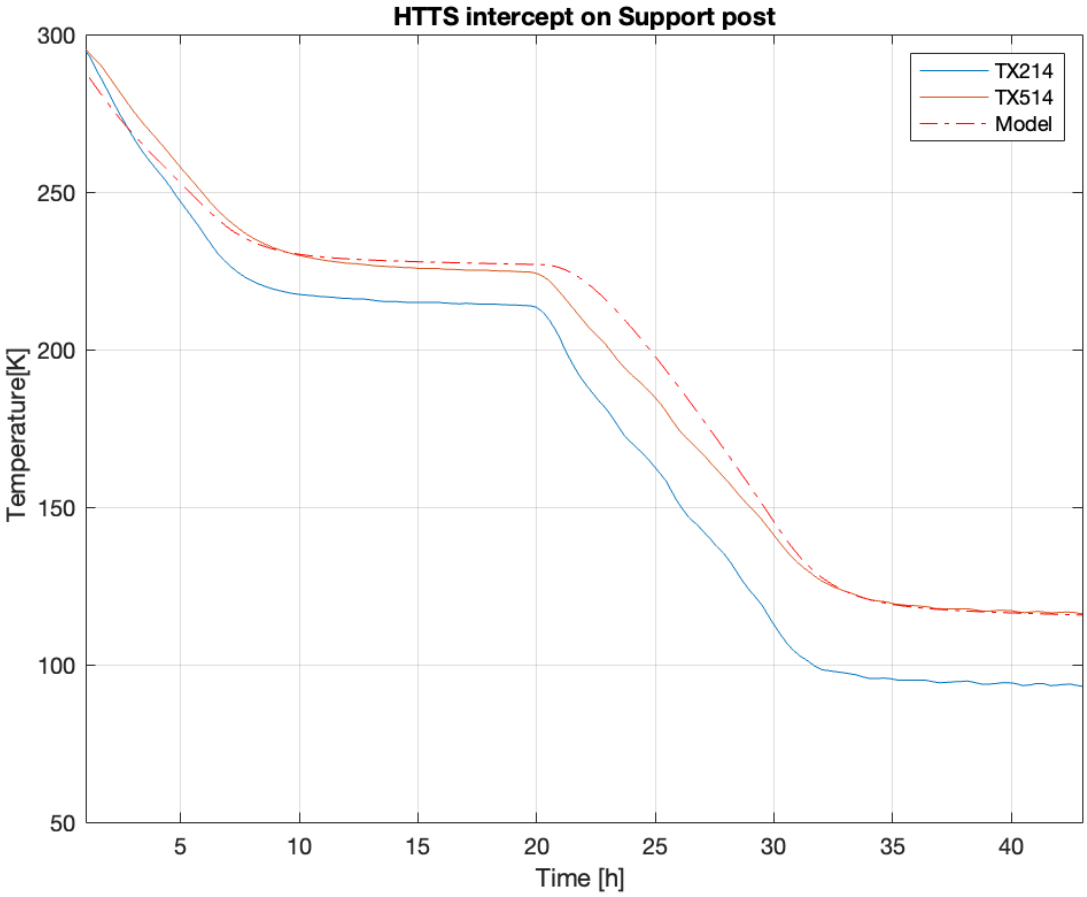

Figure 48: Validation of Support Posts in the First Part of Cool-Down.

5.1.8. Cavity

Fig. 49 presents the results obtained for the cavity during the initial phase of the cooling process. The comparison of the cavity cool down curves gives good confidence that the heat loads have been properly modelled, as the discrepancy is 4K in the initial part of the transient.

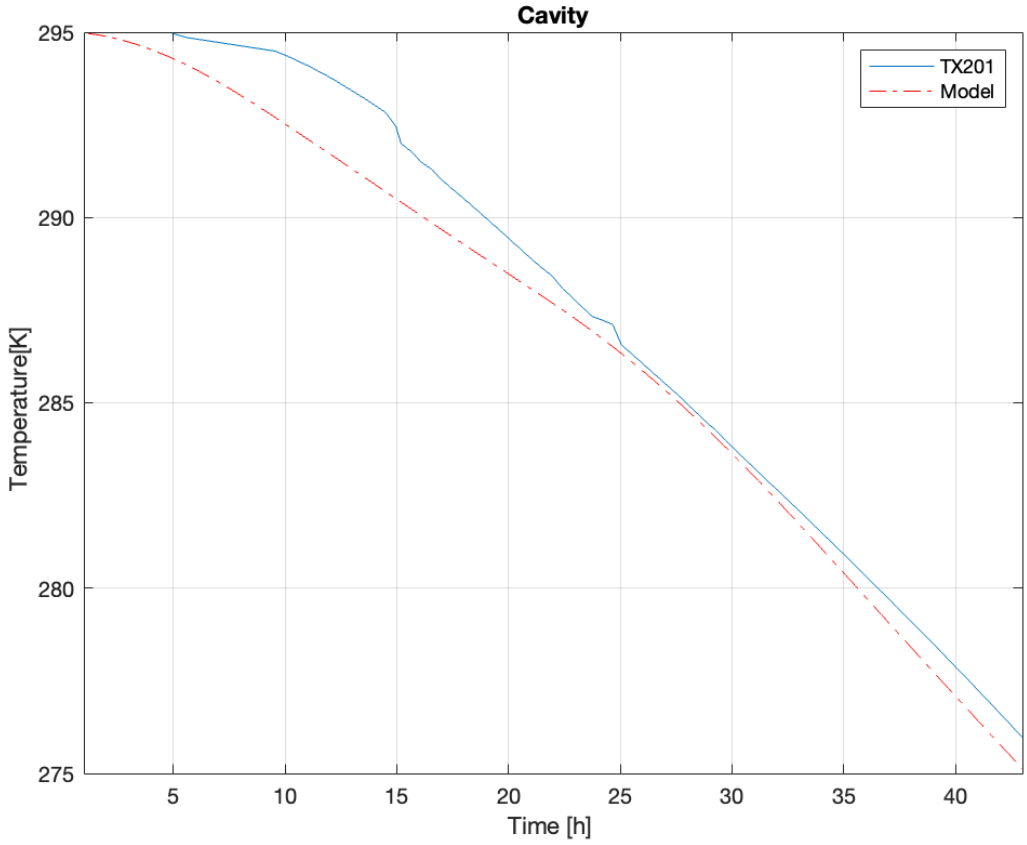

Figure 49: Validation of Cavity in the First Part of Cool-Down.

5.1.9. Strongback

Fig. 50 presents the results obtained for the strongback during the initial phase of the cooling process. The comparison of the strongback cool down curves in Fig. 50 gives good confidence that the heat loads have been properly modelled, with a discrepancy of just 0.5K.

The two sensors, TP120 and TP121, are positioned in proximity to the inlet temperature of the extruded pipe, which causes a lower temperature reading compared to other locations along the pipe. However, in the model, where every point within the extruded pipe is assumed to be at the inlet temperature, this aspect is not adequately captured.

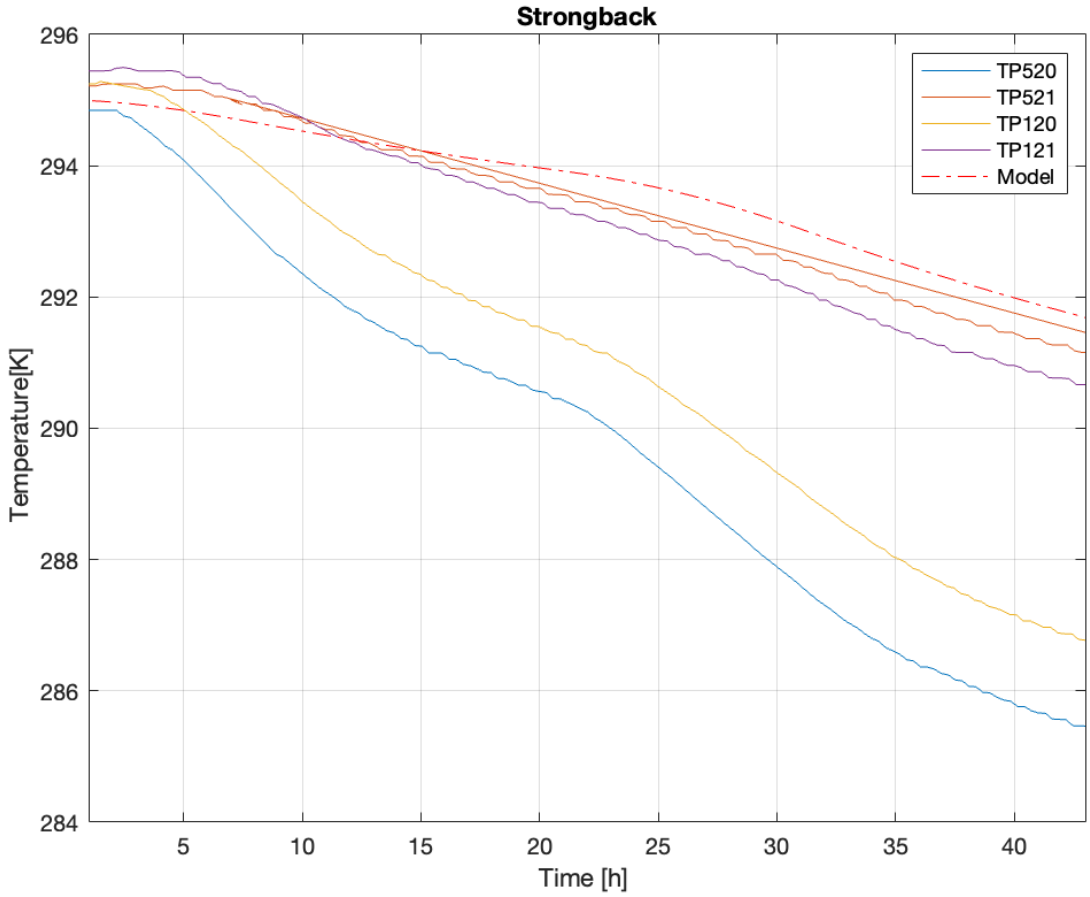

Figure 50: Validation of Strongback in the First Part of Cool-Down.

5.1.10. Relief Line

Fig. 51 presents the results obtained for the relief line during the initial phase of the cooling process within 5% on average (3% if considering only the more interesting steady state intervals). The observed mismatch in the relief line temperatures was anticipated in section 3.1, as the sensors were placed in the warmer spots along the relief line. This difference in temperature readings between the sensors and the model can be attributed to the fact that the model assumes an average (and therefore lower) temperature for the relief line. The discrepancy can be attributed to the positioning of the sensors, which captures the temperature in specific locations that may differ from the overall average temperature predicted by the model.

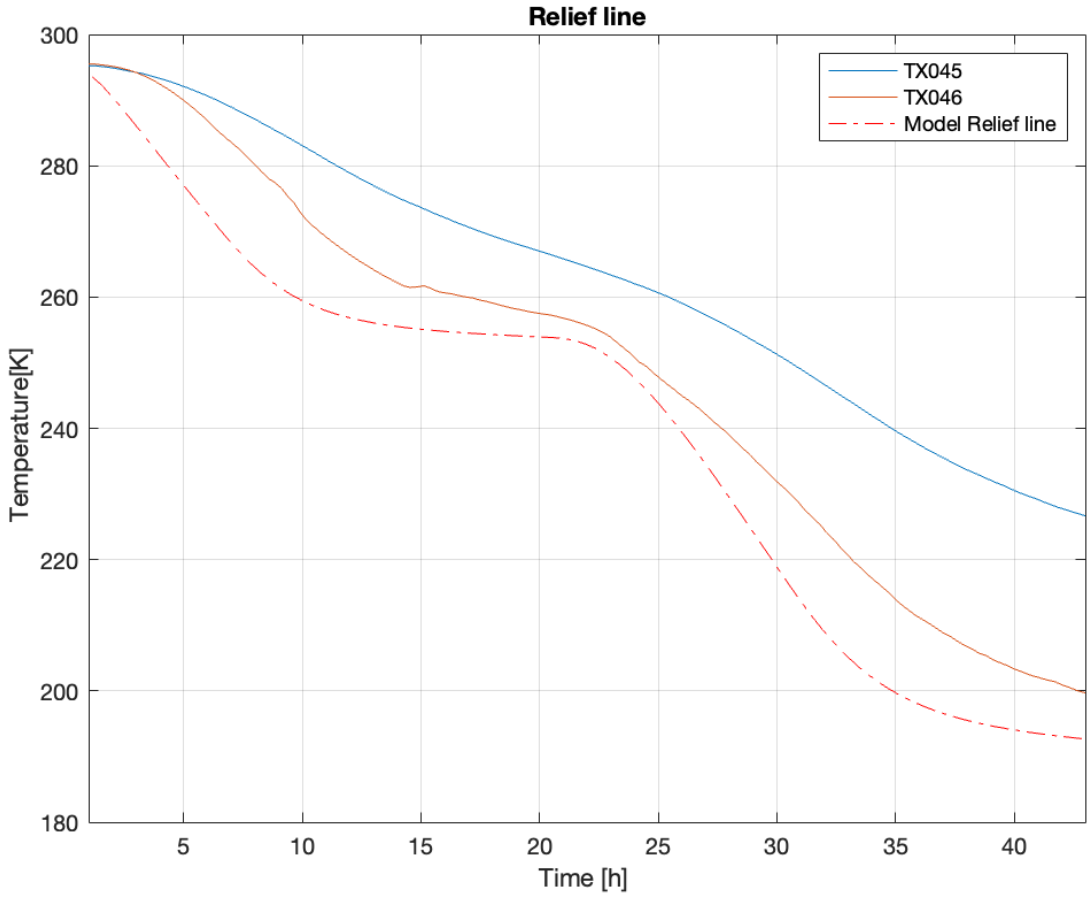

Figure 51: Validation of Relief Line in the First Part of Cool-Down.

5.2. Estimation of the Heat Loads

This paragraph presents the estimation of heat loads, specifically focusing on the static heat loads. It is important to note that the cryomodule also experiences dynamic heat loads. In the subsequent three subsections, the temperatures and average resistances utilized to determine the heat loads are provided. The temperatures mentioned are derived from Section 5.1 and represent the temperatures of the components at the conclusion of the first part of the cooling process. The average resistance is obtained by averaging the resistances calculated using the conductivity of the thermal resistance, once using the temperature of the warmer component, and another time using the temperature of the colder component.

5.2.1. Cavities

In this initial subsection, the heat loads on the cavities are calculated as they represent the coldest line and receive heat loads solely from hotter components. Although the model does not directly capture the temperature of 2K due to limited data availability, the heat loads are still calculated and evaluated at this specific temperature. Table 8 presents the average resistance, the temperature of the two components involved in the heat transfer, and the resultant heat load transferred from one coupler to one cavity.

Table 8: Coupler Heat Loads by Conduction to Cavity.

Material	Average Resistance	T (2K)	T (Coupler)	Q (W)
Copper	27	2 K	8 K	0.22
Stainless Steel	197	2 K	8 K	0.03

The cumulative static heat load originating from the coupler amounts to 0.25 W.

Table 9 presents the average resistance, the temperature of the two components involved in the heat transfer, and the resultant heat load transferred from the different kind of instrumentation to one cavity.

Table 9: Instrumentation Heat Loads by Conduction to Cavity.

Instrumentation type	Average Resistance	T (2K)	T_2	Q (W)
RF cable	1.33 e3	2 K	8 K	0.4
Heater	1.63 e4	2 K	8 K	0.3
Tuner 20 AWG	4.8 e3	2 K	8 K	0.3
PT line 1	4.8 e3	2 K	8 K	0.96
PT line 2	7.5 e3	2 K	8 K	0.16

Table 9 presents the radiative contribution from the thermal shield to the cavity, providing information on the considered emitting area and the two temperatures associated with this heat transfer.

Table 10: Radiation from Thermal Shield to Cavities.

Emitting Area	T (2K)	T (Thermal Shield)	Q (W)
35.75 m^2	2 K	57.3 K	1.8

Table 10 presents the radiative contribution from the thermal shield to the cavity, providing information on the considered emitting area and the two temperatures associated with this heat transfer.

Table 11: Radiation from Cavity Supports to Cavities.

Emitting Area	T (2K)	T (Cavity Support)	Q (W)
90 m^2	2 K	12 K	0.1

Table 11 presents the average resistance, the temperature of the two components involved in the heat transfer, and the resultant heat load transferred from a flex hose and from relief line to one cavity.

Table 12: Relief Line and Flexhoses Heat Loads by Conduction to Cavity.

Component	**Average Resistance**	**T (2K)**	**T_2**	**Q (W)**
Relief Line	5.9 e3	2K	2K	0.008
Flexhose	3.8 e3	48K	48K	0.008

The final amount of heat loads on cavities, considering the radiative and the conductive contribution, is 7 W.

5.2.2. LTTS

Table 12 presents the average resistance, the temperature of the two components involved in the heat transfer, and the resultant heat load transferred from one coupler to the LTTS.

Table 13: Coupler Heat Loads by Conduction to LTTS.

Material	Average Resistance	T (LTTS)	T (HTTS)	Q (W)
Copper	48	8 K	52 K	0.92
Stainless Steel	150.8	8 K	52 K	0.3

The combined heat loads from copper and stainless steel amount to 1.22 W. However, a portion of this heat is transferred to the cavity, as calculated in Table 7. By subtracting this heat contribution, the final net amount is determined to be 0.97 W. Table 13 presents the average resistance, the temperature of the two components involved in the heat transfer, and the resultant heat load transferred from the different kind of instrumentation to the LTTS.

Table 14: Instrumentation Heat Loads by Conduction on LTTS.

Instrumentation type	**Average Resistance**	**T (LTTS)**	**T_2**	**Q (W)**
RF cable	1.33 e3	6 K	65 K	0.044
Tuner 20 AWG	4 e3	6 K	295 K	0.07

The heat load calculated in Table 13 needs to be adjusted by subtracting the contributions listed in Table 8, as there is heat transfer from the LTTS to the cavities through wires, therefore the heat calculated via the RF cable is 0.042 W while the one via the tuner is 0.064 W. Table 14 presents the average resistance, the temperature of the two components involved in the heat transfer, and the resultant heat load transferred from support post to the LTTS.

Table 15: Support Posts Heat Loads by Conduction to LTTS.

Material	**Average Resistance**	**T (HTTS)**	**T (LTTS)**	**Q (W)**
G10	111.2	65 K	6 K	0.53

The final amount of heat loads on LTTS is 16 W.

5.2.3. HTTS

Table 15 presents the average resistance, the temperature of the two components involved in the heat transfer, and the resultant heat load transferred from the initial part of the coupler at ambient temperature to the HTTS coupler intercept.

Table 16: Coupler Heat Loads by Conduction to HTTS.

Material	**Average Resistance**	**T_{amb}**	**T (HTTS)**	**Q (W)**
Copper	116.7	293 K	52 K	2
Stainless Steel	60.1	293 K	52 K	4

The combined heat loads from copper and stainless steel amount to 6 W. However, a portion of this heat is transferred to the cavity, as calculated in Table 12. By subtracting this heat contribution, the final net amount is determined to be 5.03 W. Table 16 presents the radiative contribution from the thermal shield to the HTTS providing information on the considered emitting area and the two temperatures associated with this heat transfer.

Table 17: Radiation from Thermal Shield to HTTS.

Emitting Area	**T_{amb}**	**T (Thermal Shield)**	**Q (W)**
65.4 m^2	293 K	58 K	98

Table 17 presents the average resistance, the temperature of the two components involved in the heat transfer, and the resultant heat load transferred from the different kind of instrumentation to the HTTS.

Table 18: Instrumentation Heat Loads by Conduction on HTTS.

Instrumentation type	**Average Resistance**	**T (HTTS)**	**T_2**	**Q (W)**
RF cable	1.6 e-3	65 K	293 K	0.14

The heat load calculated in Table 17 needs to be adjusted by subtracting the contributions listed in Table 13, as there is heat transfer from the HTTS to the LTTS through wires, therefore the heat calculated via RF cable is 0.1 W.

Table 18 presents the average resistance, the temperature of the two components involved in the heat transfer, and the resultant heat load transferred from support post to HTTS.

Table 19: Support Posts Heat Loads by Conduction to HTTS.

Material	**Average Resistance**	**T_{amb}**	**T (HTTS)**	**Q (W)**
G10	144.8	293 K	65 K	1.6

The heat load calculated in Table 18 needs to be adjusted by subtracting the contributions listed in Table 14, as there is heat transfer from the HTTS to the LTTS through support post, therefore the heat calculated via support post is 1.07 W The final amount of heat loads on HTTS, considering the radiative and the conductive contribution, is 143 W.

5.2.4. Final Heat Loads Evaluation

Table 19 provides a comprehensive overview of the contributions from various components to the LTTS, HTTS, and cavities. It also includes the number of units considered for each component.

Table 20: Each Unit Heat Loads (W).

Component	HTTS	LTTS	CAVITIES	NUMBER PER UNITS
Coupler	5.03	0.97	0.25	6
Thermal Shield	98	-----	0.3	6
RF Cable	0.1	0.042	0.002	12
Heater Cable	------	----	0.02	14
Tuner 20 AWG	-----	0.064	0.006	48
Tuner PT line	-----	----	0.006	160
Tuner PT line 2	-----	----	0.04	4
Support Post	1.07	0.53	-------	12
Cavity Support	-----	-----	0.1	1
Relief Line	0.7	0.2	0.008	1
Flex hoses	-----	-----	0.008	180

Table 18 provides a straightforward calculation by multiplying the unit heat loads obtained from Table 17 by the corresponding number of components.

Table 21: Total Static Heat Loads (W).

Component	HTTS	LTTS	CAVITIES
Coupler	30.2	5.82	1.5
Thermal Shield	98	----	1.8
RF cable	1.2	0.5	0.4
Heater Cable	-----	----	0.3

Tuner 20 AWG	------	3	0.3
Tuner PT line	-----	----	0.96
Tuner PT line 2	-----	-----	0.16
Support Post	13	6.36	-----
Cavity Support	-----	-----	0.1
Relief Line	0.7	0.2	0.008
Flexhoses	-----	-----	1.44
Total	143	16	7

The results of the heat load analysis on the High-Temperature Thermal Shield (HTTS) exhibit notable differences compared to previous studies [29].

However, due to the fact that the paper containing these results has not been published yet, the detailed comparison and discussion of these findings cannot be presented in this context. It is worth noting that these differences arise from an improved calculation method for the radiation contribution, which now incorporates emissivity coefficients and view factors. Additionally, the heat load analysis for the LTTS and 2K components in the previous calculations included additional losses from various sources such as view ports, PT lines, and beam lines, resulting in higher overall heat loads. Further analysis of this cool-down process has identified additional heat sources, such as missing Multi-Layer Insulation (MLI), microphonics in the cool-down valve, and "Rollin film" within the cryogenic lines, which could not be accurately modeled using Simulink/Simscape. Ongoing efforts are dedicated to resolving these issues and conducting another cool-down of the cryomodule to validate and refine the heat load analysis. The fully detailed and comprehensive analysis of these results will be presented in the forthcoming publication.

6. Conclusions and perspective

The model for the prototype HB650 cryomodule has been developed using Simulink/Simscape and successfully validated. The model accurately predicts the transient behavior, with a relative average errors in the range of (3-10%) and the estimated heat loads at 2K is aligned with analytical calculations. This validation provides confidence in the model's ability to simulate the cryomodule's thermal performance.

Accurate estimation of heat loads is crucial in the design of cryogenic systems. By precisely calculating heat loads, various aspects can be optimized, such as the placement of thermal straps, to achieve cost and energy savings in the helium usage. In the cryogenic field, efficiency is paramount, and the ability to optimize heat loads contributes to the overall efficiency and effectiveness of the cryogenic systems.

Moving forward, the next phase of this research involves optimizing the model using data from the second cool-down of the prototype cryomodule. After the completion of the July cooldown, the obtained data will provide an opportunity to validate the model for the second and third cooldowns, enabling a comprehensive assessment of its performance across the entire cooling process. Additionally, the insights gained from this work will be applied to further refine the models for the SSR1, SSR2, and LB650 cryomodules.

This research represents a significant step towards enhancing the understanding and design of cryogenic lines. The validated model serves as a valuable tool for future studies and advancements in the field, leading to more efficient and optimized cryogenic systems in various applications.

7. References

[1] “Fermilab’s Proton Improvement Plan II will power the long-term future of the U.S. accelerator-based particle physics program and enable the world’s most powerful high-energy neutrino beam for the international Deep Underground Neutrino Experiment. PIP-II Particle Accelerator,” 2021. [Online]. Available: www.fnal.gov

[2] “Pip-II’s international engagement is the secret of Success ,” *CERN Courier*, 2021. Accessed: Jul. 04, 2023. [Online]. Available: https://cerncourier.com/a/pip-iis-international-engagement-is-the-secret-of-success/

[3] W. Chou, “SPALLATION NEUTRON SOURCE AND OTHER HIGH INTENSITY PROTON SOURCES *.”

[4] S. Belomestnykh *et al.*, “An 8 GeV Linac as the Booster Replacement in the Fermilab Power Upgrade: a Snowmass 2021 White Paper,” Mar. 2022, [Online]. Available: http://arxiv.org/abs/2203.05052

[5] V. Lebedev and / Fermi, “The PIP-II Reference Design Report,” 2015.

[6] R. Ainsworth *et al.*, “An Upgrade Path for the Fermilab Accelerator Complex,” Jun. 2021, [Online]. Available: http://arxiv.org/abs/2106.02133

[7] A. Saini, V. Lebedev, N. Solyak, and V. Yakovlev, “ESTIMATION OF CRYOGENIC HEAT LOADS IN CRYOMODULE DUE TO THERMAL RADIATION *,” 2015, doi: 10.18429/JACoW-IPAC2015-WEPTY031.

[8] C. Lhomme *et al.*, “AN APPROACH FOR COMPONENT-LEVEL ANALYSIS OF CRYOGENIC PROCESS IN SUPERCONDUCTING LINAC CRYOMODULES*,” *Proceedings of LINAC2022*, pp. 487–490, 2021, doi: 10.18429/JACoW-LINAC2022-TUPOGE04.

[9] “MathWorks Simulink.”

[10] F. Bonne, M. Alamir, C. Hoa, P. Bonnay, M. Bon-Mardion, and L. Monteiro, “A simulink library of cryogenic components to automatically generate control schemes for large cryorefrigerators,” in *IOP Conference Series: Materials Science and Engineering*, Institute of Physics Publishing, Dec. 2015. doi: 10.1088/1757-899X/101/1/012171.

[11] “Modelica.”

[12] R. Bonifetto, A. Brighenti, L. Savoldi, and R. Zanino, “Coupling superconducting magnet and refrigerator thermal-hydraulic models for nuclear fusion applications,” in *IOP Conference Series: Materials Science and Engineering*, Institute of Physics Publishing, Jun. 2019. doi: 10.1088/1757-899X/502/1/012130.

[13] S. Carli, R. Bonifetto, C. Hoa, L. Savoldi, and R. Zanino, “Thermal-hydraulic analysis of transients in the HELIOS loop including a CICC section representative of the JT-60SA Central Solenoid,” in *IOP Conference Series: Materials Science and Engineering*, Institute of Physics Publishing, Dec. 2015. doi: 10.1088/1757-899X/101/1/012147.

[14] R. Zanino, R. Bonifetto, C. Hoa, and L. S. Richard, “Verification of the predictive capabilities of the 4C code cryogenic circuit model,” in *AIP Conference Proceedings*, American Institute of Physics Inc., 2014, pp. 1586–1593. doi: 10.1063/1.4860896.

[15] F. Guelfi, R. Bonifetto, C. Hoa, L. Savoldi, and R. Zanino, “4C modeling of the supercritical helium loop HELIOS in isobaric configuration,” *Cryogenics (Guildf)*, vol. 64, pp. 51–62, 2014, doi: 10.1016/j.cryogenics.2014.09.003.

[16] R. Zanino, R. Bonifetto, C. Hoa, and L. Savoldi Richard, “4C modeling of pulsed-load smoothing in the HELIOS facility using a controlled bypass valve,” *Cryogenics (Guildf)*, vol. 57, pp. 31–44, Oct. 2013, doi: 10.1016/j.cryogenics.2013.04.005.

[17] R. Zanino, R. Bonifetto, F. Casella, and L. Savoldi Richard, “Validation of the 4C code against data from the HELIOS loop at CEA Grenoble,” in *Cryogenics*, Jan. 2013, pp. 25–30. doi: 10.1016/j.cryogenics.2012.04.010.

[18] R. Bonifetto, F. Casella, L. Savoldi Richard, and R. Zanino, “Dynamic modeling of a supercritical helium closed loop with the 4C Code,” in *AIP Conference Proceedings*, 2012, pp. 1743–1750. doi: 10.1063/1.4707109.

[19] V. Roger *et al.*, “Design of the 650 MHz High Beta Prototype Cryomodule for PIP-II at Fermilab,” United States, 2022. doi: 10.18429/JACoW-SRF2021-WEPTEV015.

[20] E. Urquiza, C. Vasquez, J. Rodriguez, and B. Van Gorp, “Development and testing of an innovative two-arm focal-plane thermal strap (TAFTS),” *Cryogenics (Guildf)*, vol. 52, no. 4–6, pp. 306–309, Apr. 2012.

[21] R. C. Dhuley, M. Ruschman, J. T. Link, and J. Eyre, “Thermal conductance characterization of a pressed copper rope strap between 0.13 K and 10 K,” *Cryogenics (Guildf)*, vol. 86, pp. 17–21, Sep. 2017, doi: 10.1016/j.cryogenics.2017.07.001.

[22] S. V. Kutsaev, M. P. Kelly, and P. N. Ostroumov, “Design of RF power coupler for superconducting cavities,” *Journal of Instrumentation*, vol. 7, no. 11, Nov. 2012, doi: 10.1088/1748-0221/7/11/P11004.

[23] M. White *et al.*, “Cryogenic system for the cryomodule test facility at fermilab,” in *AIP Conference Proceedings*, American Institute of Physics Inc., 2014, pp. 179–186. doi: 10.1063/1.4860699.

[24] V. Roger, S. Chandrasekaran, and D. Passarelli, “DESIGN STRATEGY OF THE PIP-II CRYOMODULES *,” 2019, doi: 10.18429/JACoW-SRF2019-MOP094.

[25] V. Roger *et al.*, “STANDARDIZATION AND FIRST LESSONS LEARNED OF THE PROTOTYPE HB650 CRYOMODULE FOR PIP-II AT FERMILAB*,” 2021, doi: 10.18429/JACoW-LINAC2022-TUPOGE16.

[26] THEODORE L. BERGMAN, ADRIENNE S. LAVINE, FRANK P. INCROPERA, and DAVID P. DEWITT, *Introduction to Heat Transfer*. 1981.

[27] E. D. Marquardt, J. P. Le, and R. Radebaugh, "Cryogenic Material Properties Database," in *Cryocoolers 11*, Springer US, 2002, pp. 681–687. doi: 10.1007/0-306-47112-4_84.

[28] "Radiative Heat Transfer Block."

[29] V. Roger, "HB650 cryomodule design: from prototype to production," in *SRF'21*, Michigan state university, USA.

Appendix

.

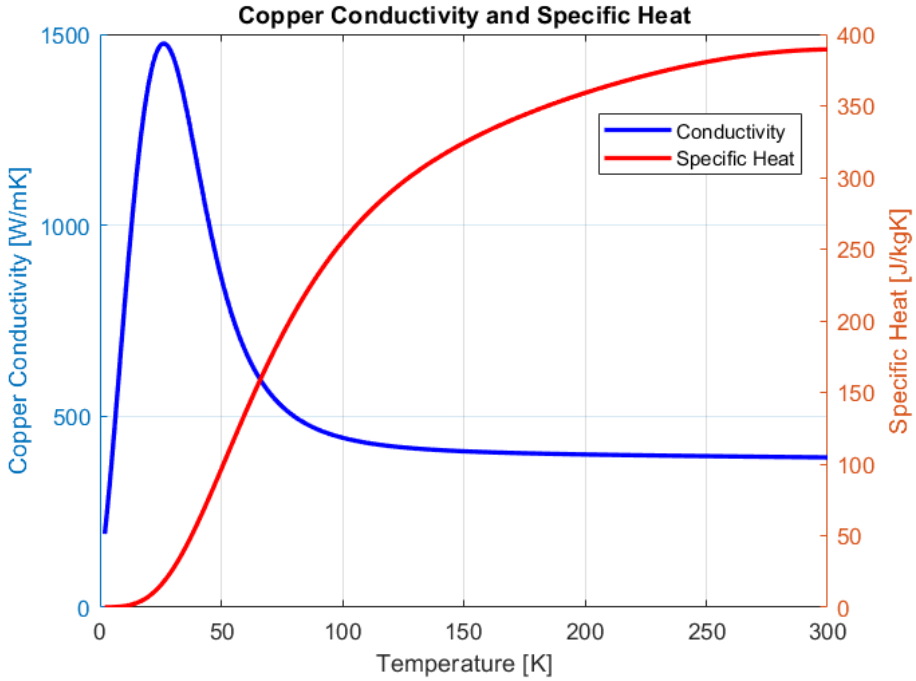

Figure 52: Copper Specific Heat and Conductivity.

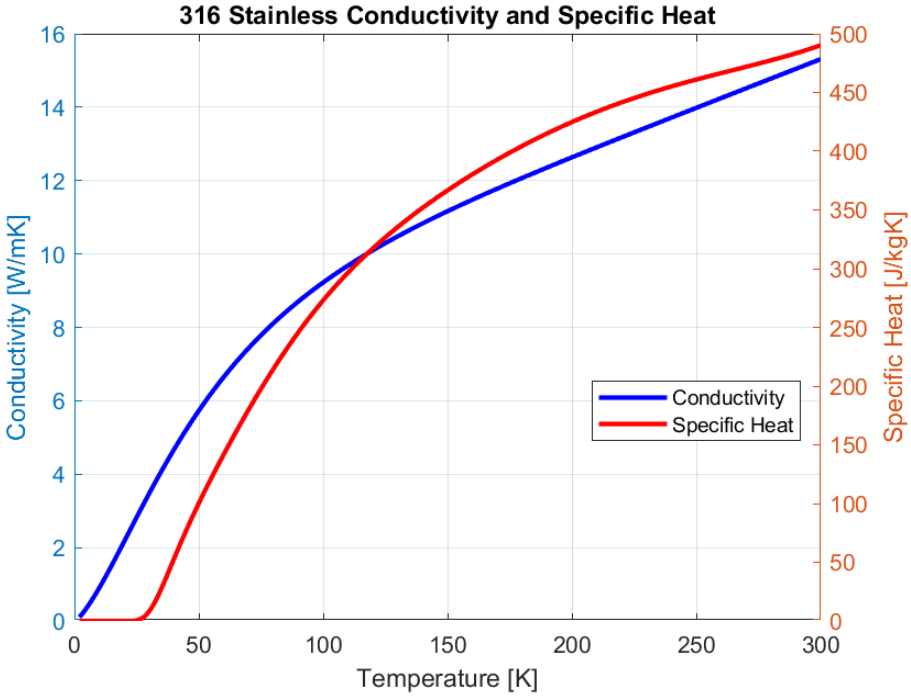

Figure 53: 316 Stainless Steel Specific Heat and Conductivity.

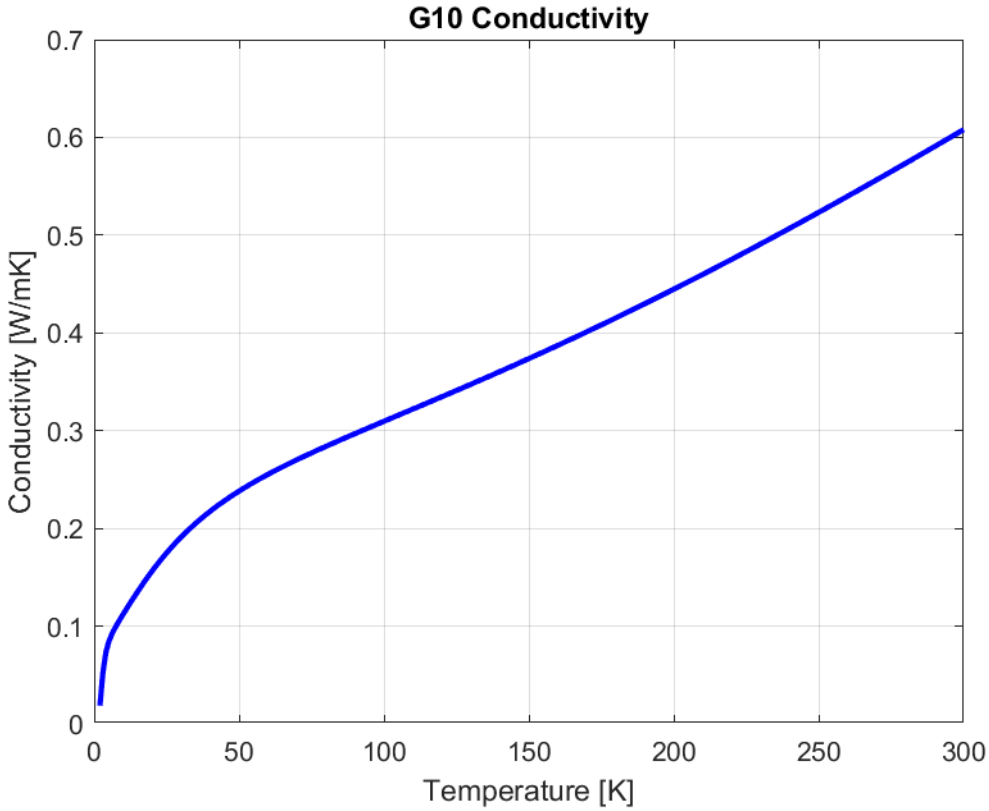

Figure 54: G10 Conductivity.

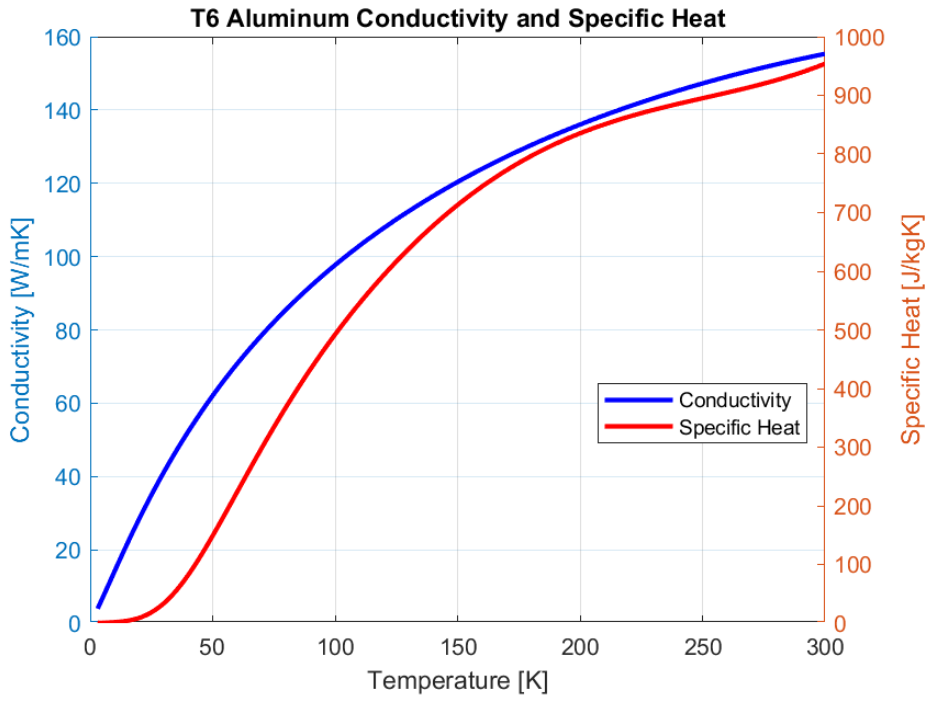

Figure 55: T6 Alliminum Conductivity and Specific Heat.